nature materials

Article

https://doi.org/10.1038/s41563-026-02553-2

Mechanisms of active wetting and fluidification in epithelial cell collectives

Received: 11 February 2025

Accepted: 20 February 2026

Published online: 23 March 2026

Check for updates

Stefano Marchesi[1], Chiara Guidolin[2], Andrew E. Massey[3], Gregoire Lemahieu[4], Zeno Lavagnino[1], Galina V. Beznoussenko[1], Alexandre A. Mironov[1], Brenda J. Green[1,5], Elisa Allievi[1], Emanuele Martini[1,5], Serena Magni[1], Andrea Ghisleni[1,10], Caterina Lomazzi[2], Andrea Francesco Benvenuto[6], Andreas Schertel[7], Diana A. van Faassen[1,8], Stefano Freddi[5,6], Giovanni Bertalot[6,11,12], Dario Parazzoli[1], Paolo Maiuri[1,13], Marina Mapelli[6], Salvatore Pece[5,6], Sara Sigismund[5,6], Nils C. Gauthier[1], Elisabetta A. Cavalcanti-Adam[4,9], Alexander X. Cartagena-Rivera[3,14], Fabio Giavazzi[2,14], Giorgio Scita[1,5,14] ✉ & Andrea Disanza[1,5,14]

Tissue-level phase transitions are emerging as a crucial mechanism in tumour development and metastasis. When becoming invasive, epithelial tumours undergo a transition from a solid-like state to a more fluid-like one. Although the contributions of cell adhesions, traction forces and cell migration for such behaviour are known, the exact biophysical and molecular mechanisms controlling these transitions are not fully understood. Here we show that breast cancer cell fluidity is regulated by IRSp53, a protein linking plasma membranes to the cytoskeleton. In both two-dimensional monolayers and three-dimensional spheroids, the depletion of IRSp53 increases fluidity and active wetting of the substrate due to a decrease in intercellular friction and enhanced local cell rearrangements. Molecularly, IRSp53 interacts with the junctional protein Afadin to control global tensile state and active wetting, establishing these proteins as key regulators of epithelial collectives' viscosity in breast cancer tumouroids. In breast cancer patient samples, low IRSp53 expression levels and aberrant localization correlate with worse clinical outcomes. These findings support the broader relevance of IRSp53-regulated mechanics in epithelia and their potential prognostic value in cancer.

Alterations in the mechanical properties of single cells and tissues are increasingly recognized as hallmarks of disease, particularly cancer. Mechanical features such as tension, adhesion, elasticity and viscosity are governed by actomyosin cytoskeletal dynamics and transmitted across tissues through cell–cell and cell–extracellular matrix (ECM) adhesions[1–3].

At the tissue scale, physical phase transitions—most notably, solid-to-fluid-like behaviours and active wetting—are emerging as key regulators of morphogenesis and disease progression[4–10]. Epithelial tissues often adopt a solid-like, jammed state at high density due to coordinated adhesion, cortical tension and constrained cell motility[10]. This jammed state is tumour suppressive, as it maintains tissue cohesion and limits the emergence of invasive clones[5,11,12]. Conversely, alterations in adhesion, cell shape or contractility can promote tissue fluidization, facilitating transitions from indolent ductal carcinoma in situ (DCIS) to invasive disease[5,11,12].

Transitions between three-dimensional spheroids and two-dimensional monolayers provide an experimentally tractable

A full list of affiliations appears at the end of the paper. ✉e-mail: giorgio.scita@ifom.eu

framework to study these processes, particularly in the context of active epithelial wetting[5,6]. Unlike passive wetting, active wetting arises from the balance between cell-generated traction forces and intercellular contractility and is well captured by active polar fluid models[9,13]. Despite remarkable theoretical progress, the molecular mechanisms controlling these tissue-level phase transitions remain poorly understood.

Here we investigate the role of IRSp53, a membrane-associated I-BAR domain protein that links membrane curvature sensing to actin cytoskeletal regulation[14–16]. IRSp53 promotes directional migration by inducing the formation of filopodia and lamellipodia[15,17,18], which have also been implicated in shaping cell–cell adhesions in epithelia[19,20]. Consistent with this, IRSp53 localizes at cell–cell contacts[21–23], regulates integrin trafficking[24], and is required for the polarized architectural organization and morphogenesis of epithelial tissues[21]. These properties position IRSp53 as a candidate regulator of epithelial mechanics at the interface between membrane remodelling and cytoskeletal force transmission.

Using MCF10DCIS.com cells as a model for early breast cancer[25], we show that IRSp53 depletion disrupts coordinated collective migration in two-dimensional (2D) monolayers and delays jamming transitions at high cell density. By contrast, the loss of IRSp53 enhances the spreading of three-dimensional (3D) spheroids, indicating a primary effect on epithelial collectives' viscosity rather than cell–substrate adhesion. Combining live imaging, biophysical measurements and theoretical modelling, we demonstrate that these effects arise from reduced supracellular tension, altered junctional organization and increased fluidity of epithelial collectives. At the molecular level, we identify Afadin (AFD) as a functional interactor of IRSp53. AFD is essential for epithelial development, polarity and cortical tension regulation[26–30], and its depletion recapitulates IRSp53-loss phenotypes in wetting assays. Together, our findings identify IRSp53 and AFD as key regulators of epithelial viscoelasticity, linking junctional architecture and single-cell mechanics to tissue-scale phase transitions relevant to tumour progression.

Consistent with this framework, the analysis of patient datasets reveals that the reduced expression and aberrant localization of IRSp53 correlate with a poor clinical outcome in breast cancer, underscoring the pathological relevance of IRSp53-regulated tissue mechanics.

IRSp53 removal affects DCIS collective motion

IRSp53 regulates the interplay between the plasma membrane and the actin cytoskeleton during directional migration and invasion, contributes to cell–cell and cell–ECM adhesions, and is required for the polarized organization of epithelial tissues[14–18,31]. Perturbation of these processes is associated with invasive breast cancer and the emergence of collective migratory behaviours[32].

To investigate the role of IRSp53 in this context, we generated inducible shRNA-expressing MCF10DCIS.com cells to downregulate IRSp53 (Fig. 1a). This cell line models early breast cancer progression, as it forms ductal-carcinoma-like structures that can evolve into invasive tumours in vivo[25]. MCF10DCIS.com cells retain epithelial characteristics, including E-cadherin-based junctions and the ability to form dense, jammed monolayers and exhibiting partial mesenchymal traits[12].

We first examined collective migration during wound healing in confluent monolayers. IRSp53 depletion had minimal effects on the initial rate of wound closure (Fig. 1b, early phase, and Supplementary Video 1). However, it significantly reduced the long-range coordination of cell motion, as evidenced by the decreased correlation length and reduced directionality of single-cell trajectories (Fig. 1b, Extended Data Fig. 1a and Supplementary Videos 1 and 2). These defects resulted in delayed wound closure at later time points. The re-expression of murine IRSp53, resistant to the shRNA, fully rescued coordinated migration and wound closure dynamics (Fig. 1a,b).

In particular, IRSp53 loss did not affect the migration of isolated cells in one-dimensional linear motility assays (Extended Data Fig. 1b and Supplementary Video 3), indicating that IRSp53 primarily regulates emergent collective properties rather than intrinsic single-cell motility. Loss of coordination was observed not only at the wound edge but also deep within the monolayer (Supplementary Video 4), suggesting a defect in long-range mechanical or polarity coupling across the cell collective.

Dense epithelial monolayers undergo a fluid-to-solid (jamming) transition as proliferation increases crowding and constrains cell motion[10]. We, therefore, tested whether IRSp53 contributes to this transition. Although control monolayers progressively arrested their motion, IRSp53-depleted monolayers remained fluid-like, displaying sustained velocity fluctuations at late time points. This was quantified by an increased root mean square velocity ($V_{\mathrm{r.m.s.}}$), measured by both particle image velocimetry (PIV) and single-cell tracking (Fig. 1c, Extended Data Fig. 1c and Supplementary Video 5). Importantly, IRSp53 depletion did not alter the proliferation rates, as nuclear density increased similarly in control and knockdown monolayers (Extended Data Fig. 1d), indicating that delayed jamming was not due to differences in cell growth.

Previous work demonstrated that the expression of the endocytic protein RAB5A reawakens motility in jammed epithelial monolayers by inducing long-range coordinated flocking motion[7,12,33]. We, therefore, asked whether IRSp53 is required for RAB5A-induced collective migration. As expected, RAB5A expression promoted highly coordinated multicellular streams, quantified by an increase in the velocity of the centre of mass (V_{CM}) (Fig. 1d, Extended Data Fig. 1e and Supplementary Video 6). Notably, silencing IRSp53 in RAB5A-expressing monolayers severely impaired the flocking behaviour, resulting in a marked reduction in V_{CM} despite preserved RAB5A expression.

Together, these data demonstrate that IRSp53 is dispensable for single-cell migration but is essential for long-range coordination of collective motion, the establishment of a jammed state at high density and the emergence of coherent flocking dynamics in epithelial monolayers.

IRSp53 loss decreases epithelial collective viscosity

To identify the physical parameters controlled by IRSp53 during collective dynamics, we investigated the active wetting behaviour of epithelial spheroids, a well-established system to probe active tissue fluidization[6,9,13]. In this assay, 3D spheroids spread onto adhesive substrates, transitioning into 2D monolayers through an active wetting process.

Time-lapse microscopy revealed that IRSp53 depletion markedly accelerated spheroid spreading compared with control spheroids (Fig. 2a, Extended Data Fig. 1f and Supplementary Videos 7 and 8). This effect was reproduced in primary murine mammary epithelial cells lacking IRSp53 as well as in human HaCat keratinocytes with inducible IRSp53 knockdown (Extended Data Fig. 1g–h and Supplementary Videos 9 and 10), indicating a general role for IRSp53 in regulating wetting dynamics.

In analogy with liquid droplets, the spreading of cell aggregates reflects a balance between cell–cell cohesion and traction forces exerted on the substrate[6,9]. Given that IRSp53 depletion impaired coordinated migration in wound-healing assays (Fig. 1b), it was unlikely that enhanced spreading resulted from increased cell–substrate adhesion. We, therefore, hypothesized that IRSp53 primarily regulates collective viscosity and cohesion.

Both control and IRSp53-depleted spheroids spread at approximately constant rates of $\frac{dA}{dt}$; however, the spreading rate was significantly higher on IRSp53 knockdown (Fig. 2a). To gain a mechanistic insight, we quantified the time-resolved velocity fields of spreading spheroids using PIV. Radial velocity profiles displayed a characteristic non-monotonic shape, with a maximum near the spreading front (Fig. 2b), consistent with predictions of active polar fluid theory[9].

https://doi.org/10.1038/s41563-026-02553-2

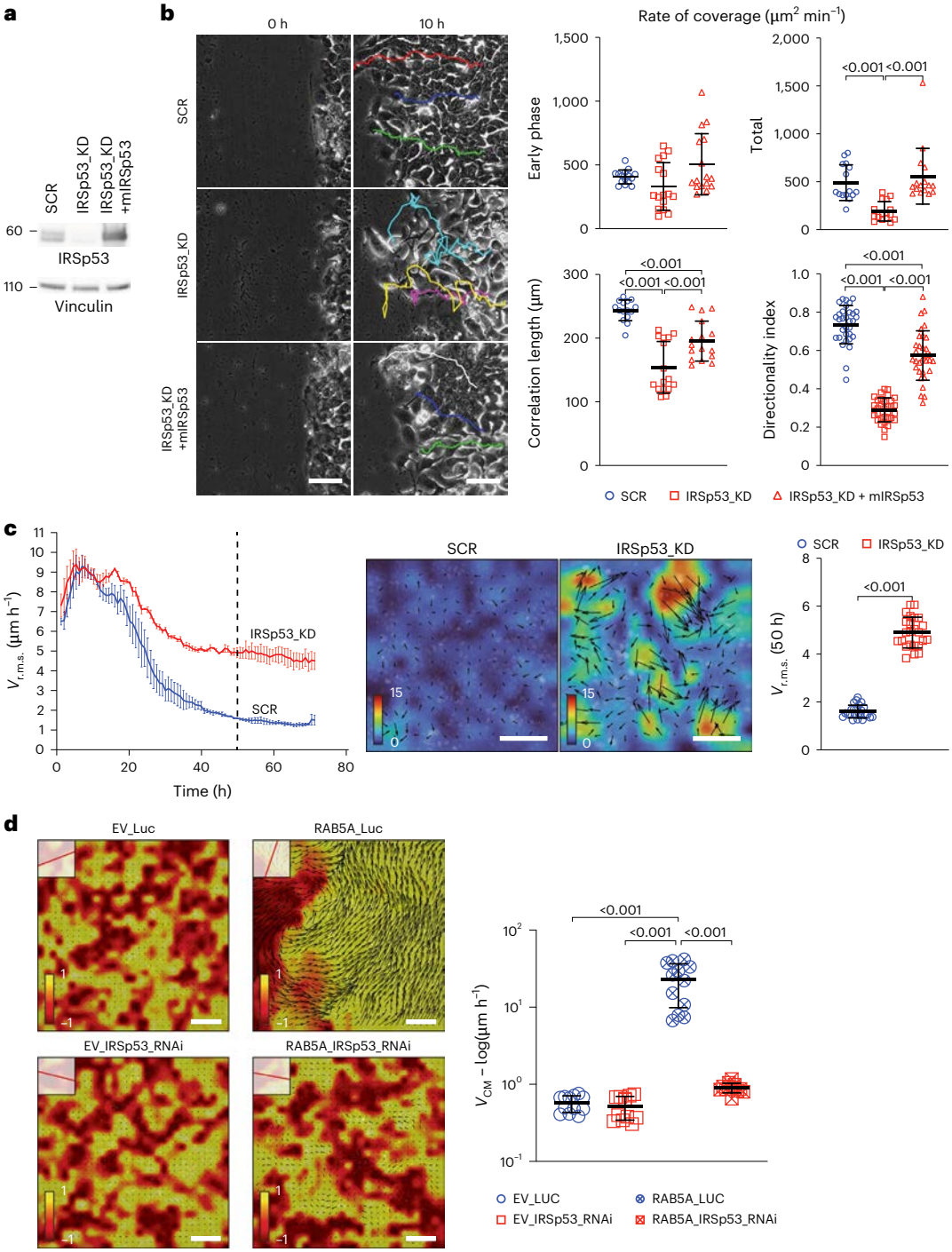

Fig. 1 | IRSp53 removal affects DCIS collective motion. a, Immunoblotting of MCF10DCIS.com SCR, IRSp53_KD and IRSp53_KD rescued with murine IRSp53 (IRSp53_KD + mIRSp53) using the indicated antibodies. **b**, Scratch-wound migration of SCR, IRSp53_KD and IRSp53_KD + mIRSp53 monolayers (Supplementary Video 1). Left: representative still images at the indicated times. Scale bar, 100 μm. Right: motility quantification. Top: wound coverage rate, measured as % area covered over time (early phase = first 2 h of active migration). Bottom left: velocity correlation length from PIV. Mean ± s.d. (≥15 fields of view; three independent experiments). Bottom right: directionality index from manual tracking of leading-edge cells in ImageJ (example trajectories shown). Mean ± s.d. (n = 32 cells; three independent experiments). **c**, Left: PIV-derived root mean square velocity ($V_{r.m.s.}$) over time for SCR-H2B-GFP and IRSp53_KD-H2B-mCherry MCF10DCIS.com cells seeded at the jamming density and monitored by time-lapse microscopy (Supplementary Video 5). Mean ± s.d. (>20 fields; three independent experiments). The vertical dashed line indicates the time point (t = 50 h) corresponding to the snapshots shown beside. Centre: dashed line marks t = 50 h, corresponding to the velocity-field snapshots shown. Scale bar, 100 μm. Right: $V_{r.m.s.}$ at t = 50 h. Mean ± s.d. (>20 fields from three independent experiments). **d**, Left: representative PIV velocity-field snapshots at t = 20 h for empty vector (EV) or RAB5A cells, transfected with control oligos (Luc, EV_Luc, RAB5A_Luc) or human IRSp53 siRNA (EV_IRSp53_RNAi, RAB5A_IRSp53_RNAi), seeded at the jamming density and imaged by time-lapse microscopy (Supplementary Video 6). The colour map reflects the alignment with respect to the mean velocity $\mathbf{v}_{CM}$, quantified by the parameter $a(x) = \mathbf{v}(x) \cdot \mathbf{v}_{CM}/||\mathbf{v}(x)||||\mathbf{v}_{CM}||$. A value $a = 1$ ($a = -1$) indicates that the local velocity is parallel (antiparallel) to the mean direction of migration, indicated by the red line in the top-left square of each snapshot. Scale bar, 200 μm. Right: collective motion velocity V_{CM} shown in the log scale. Mean ± s.d. (n = 12 fields; two independent experiments). IRSp53 and RAB5A expressions were verified using quantitative reverse-transcription polymerase chain reaction (Extended Data Fig. 1e). Statistical tests are listed in Supplementary Table 4; the P values are shown in the graphs.

https://doi.org/10.1038/s41563-026-02553-2

We modelled the spreading monolayer as a two-dimensional active polar fluid characterized by a polarity field **p** and a velocity field **v**. Under the adiabatic approximation, the polarity field obeys the steady-state equation

$$L_c^2 \nabla^2 p_\alpha = p_\alpha, \quad (1)$$

where L_c is the nematic length. In the low-Reynolds-number limit, force balance requires that traction stresses exerted on the substrate balance gradients of the internal stress tensor σ^s/h:

$$\frac{1}{h}\partial_\beta \sigma^s_{\alpha\beta} = T_\alpha, \quad (2)$$

where h is the monolayer thickness and σ^s is symmetric part of the stress tensor. The antisymmetric part, consistent with the adiabatic approximation for the polarity field, is assumed to be negligible. The model is complemented with the following simplified constitutive equations:

$$\sigma^s_{\alpha\beta} = \eta\left(\partial_\alpha v_\beta + \partial_\beta v_\alpha\right) - \zeta p_\alpha p_\beta \quad (3)$$

and

$$T_\alpha = -T_0 p_\alpha \quad (4)$$

are the internal stress and the traction stress, respectively. In previous equations, T_0 represents the maximum traction stress, which quantifies the maximum force per unit area exerted by cells on the substrate; $\zeta < 0$ is the active stress coefficient or contractility, which is related to the active contractile forces within the epithelial collective, driven by molecular motors like myosin; and η is the monolayer viscosity, representing its resistance to flow (Fig. 2b). Remarkably, as shown before[9], the model can be analytically solved in a circular geometry, assuming purely radial polarization and velocity fields. The circular monolayer (or radius R) is assumed to be fully polarized at the boundaries, leading to the boundary condition $p_r(R) = 1$ for the radial component of the polarity field, whereas symmetry considerations impose $p_r(0) = 0$ at the centre. Similarly, the radial component of the velocity field is assumed to vanish at the centre ($v_r(0) = 0$), whereas stress-free boundary conditions ($\sigma_{rr}(R) = 0$) are imposed on the free edge of the monolayer.

To account for the presence of a persistent solid core at the centre of spreading spheroids, we solved the model in an annular geometry of external radius R and internal radius R_1, corresponding to the size of the stiff core. Consistently, at the internal boundary, we assume $v_r(R_1) = 0$ and $p_r(0) = 0$, whereas the conditions at the external boundary are the same as in ref. 9 (Methods). The analytical solution accurately fitted the experimental radial velocity profiles, $v_r(r)$ (Fig. 2b), and enabled the extraction of a combination of physical parameters, namely, $A \equiv T_0/\eta h$ and $B \equiv -\frac{\zeta}{\eta}$, and the nematic length L_c (Fig. 2c, d and Extended Data Fig. 1i,j).

A major difference between conditions emerged in the dynamics of the solid core. In control spheroids, the normalized core radius remained nearly constant over time, whereas IRSp53-depleted spheroids displayed a rapid dissolution of the core (Fig. 2c). A quantification of the melting rate confirmed significantly faster fluidization on IRSp53 loss (Fig. 2d), accounting for the increased spreading rate.

Model fitting further revealed that IRSp53 depletion increased both traction-to-viscosity ratio and contractility-to-viscosity ratio ($T_0/\eta h$ and $-\frac{\zeta}{\eta}$, respectively) (Fig. 2e,f), whereas the nematic length showed only minor differences (Extended Data Fig. 1j), indicating that the loss of IRSp53 in spreading spheroids impacts both ratio between traction forces exerted on the substrate and viscosity and the ratio between cell collective contractility and viscosity. The ratio $\mathrm{B/A} = -\frac{\zeta h}{T_0}$ exhibits a reduction on IRSp53 knockdown (Extended Data Fig. 1k), indicating that IRSp53 loss alters the balance between internal tension and substrate coupling independently of viscosity. We extended the analysis to spheroids of different sizes. In these conditions, the area growth rate depends on the initial spheroid size but a significant difference between SCR and IRSp53_KD is conserved in terms of $\frac{dA}{dt}$ (Extended Data Fig. 2a), $T_0/\eta h$ and $-\frac{\zeta}{\eta}$ (Extended Data Fig. 2b,c) with no significant behaviour in L_c (Extended Data Fig. 2d).

To directly test whether traction forces were affected, we performed traction force microscopy during spheroid spreading. Radial traction profiles decayed monotonically from the edge towards the centre (Fig. 2g and Supplementary Video 11), in excellent agreement with model predictions. Neither maximum traction stress nor nematic length differed significantly between control and IRSp53-depleted spheroids (Fig. 2h–j). Additionally, the L_c estimates were consistent with values independently derived from PIV data (Fig. 2j and Extended Data Fig. 1j). Thus, our results demonstrate that traction force generation is largely preserved.

Consistent with this conclusion, traction forces measured in the inner and outer regions of the spreading spheroids were unchanged (Extended Data Fig. 2e). IRSp53 depletion did not alter the focal adhesion number or size (Extended Data Fig. 2f), which have been shown to be directly dependent on the forces exerted to the substrate[34] and not the surface levels of total or active β1-integrin (Extended Data Fig. 2g). The latter results imply that IRSp53 is not, or only marginally, involved in β1-integrin trafficking in our DCIS cellular system, at variance with results obtained in different cell models[24].

Fig. 2 | IRSp53 loss decreases cell spheroid viscosity. a, Representative still images from the time-lapse images of SCR or IRSp53_KD MCF10DCIS.com spheroids seeded on fibronectin-coated six-well plates (Supplementary Video 7). Scale bar, 200 µm. Left graph: spreading area quantified manually (ImageJ). Mean ± s.d. (n = 21 SCR, 20 IRSp53_KD spheroids; three independent experiments). Right graphs: semiautomatic segmentation of area versus time shows faster spreading on IRSp53 knockdown. Mean ± s.d. (n = 7 SCR, 5 IRSp53_KD spheroids). Solid black lines, linear fits with slopes $dA/dt = (1.27 \pm 0.19) \times 10^4$ µm^2 h^{-1} for SCR and $dA/dt = (4.77 \pm 0.33) \times 10^4$ µm^2 h^{-1} for KD. Box chart: dA/dt values of a single spheroid. Mean ± s.d. (n = 16 SCR, 11 IRSp53_KD spheroids; three independent experiments). **b**, Model framework. Left: monolayer internal stress contributions—active contractile stress (amplitude $-\zeta$, linked to the polarity field) and viscous stress (amplitude η, linked to velocity gradients). Middle (top): spreading geometry defining the initial size R_0 (equivalent radius at $t = 0$), monolayer radius R, thickness h and stiff-core radius R_1 (radial velocity expected to vanish). Velocity **v** and traction **T** fields are indicated. Middle (bottom): radial velocity and predicted traction profiles. v_r intersects the x axis in R_1; initial slope $\approx \frac{T_0 L_c}{\eta h}$; slope at $r = R \approx \frac{\zeta}{\eta}$; velocity peak occurs at $\simeq L_c$ from the boundary. Predicted traction profile T_r has a peak amplitude T_0 and characteristic length L_c (nematic length). Top right: example at t = 24 h of an IRSp53_KD spheroid—top view with a segmented area (red) and the corresponding PIV velocity field (colour map, µm h^{-1}). Scale bar, 200 µm. Bottom right: representative azimuthally averaged v_r profiles over time for SCR and IRSp53_KD. Mean ± s.d. over five consecutive frames. Model fits yield viscosity- and contractility-related parameters. **c**, Time evolution of core size R_1/R_0: approximately constant in SCR but rapidly decreases in IRSp53_KD, indicating faster core 'melting'. Mean ± s.d. (n = 7 SCR, 5 IRSp53_KD). **d**, Core-melting rate $d(R_1/R_0)/dt$ from linear fits of single spheroids. Mean ± s.d. (n = 15 SCR, 11 IRSp53_KD; three independent experiments). **e**,**f**, Fit parameters A (e) and B (**f**) from radial velocity profiles evaluated at matched spreading. A, traction to viscosity (T_0/η); B, contractility to viscosity (ζ/η). Mean ± s.d. (n = 16 SCR, 11 IRSp53_KD; three independent experiments). **g**, Traction force microscopy. Left: segmentation and traction map of an IRSp53_KD spheroid (colour map, kPa). Scale bar, 50 µm. Right: representative radial traction profiles over time for SCR and IRSp53_KD. Solid lines, best fits. **h**, Average evolution of the maximum traction T_0 over time for SCR (blue line) and IRSp53_KD (red line). **i**,**j**, T_0 (**i**) and L_c (**j**) evaluated at matched spreading (the front has doubled: $R = (2.0 \pm 0.2)R_0$). Mean ± s.d. (n = 29 SCR, 28 IRSp53_KD spheroids; three independent experiments). No significant difference in L_c or T_0 is observed. Statistical tests are listed in Supplementary Table 4; the P values are shown in the graphs.

https://doi.org/10.1038/s41563-026-02553-2

Enhanced spreading was also observed on laminin- and collagen-coated substrates (Extended Data Fig. 2h,i and Supplementary Video 12), excluding matrix-specific effects.

Together, these results demonstrate that IRSp53 controls epithelial spheroid spreading primarily by regulating collective viscosity and contractility, promoting solid-core dissolution and fluidization during active wetting. The contribution of tissue geometry to IRSp53-dependent collective migration, and its impact on force alignment and collective dynamics, is discussed in the Supplementary Discussion.

Experimental validation of IRSp53 in epithelial viscosity

To experimentally validate the role of IRSp53 in regulating epithelial collective viscosity, we used complementary approaches probing spheroid mechanics across distinct deformation regimes.

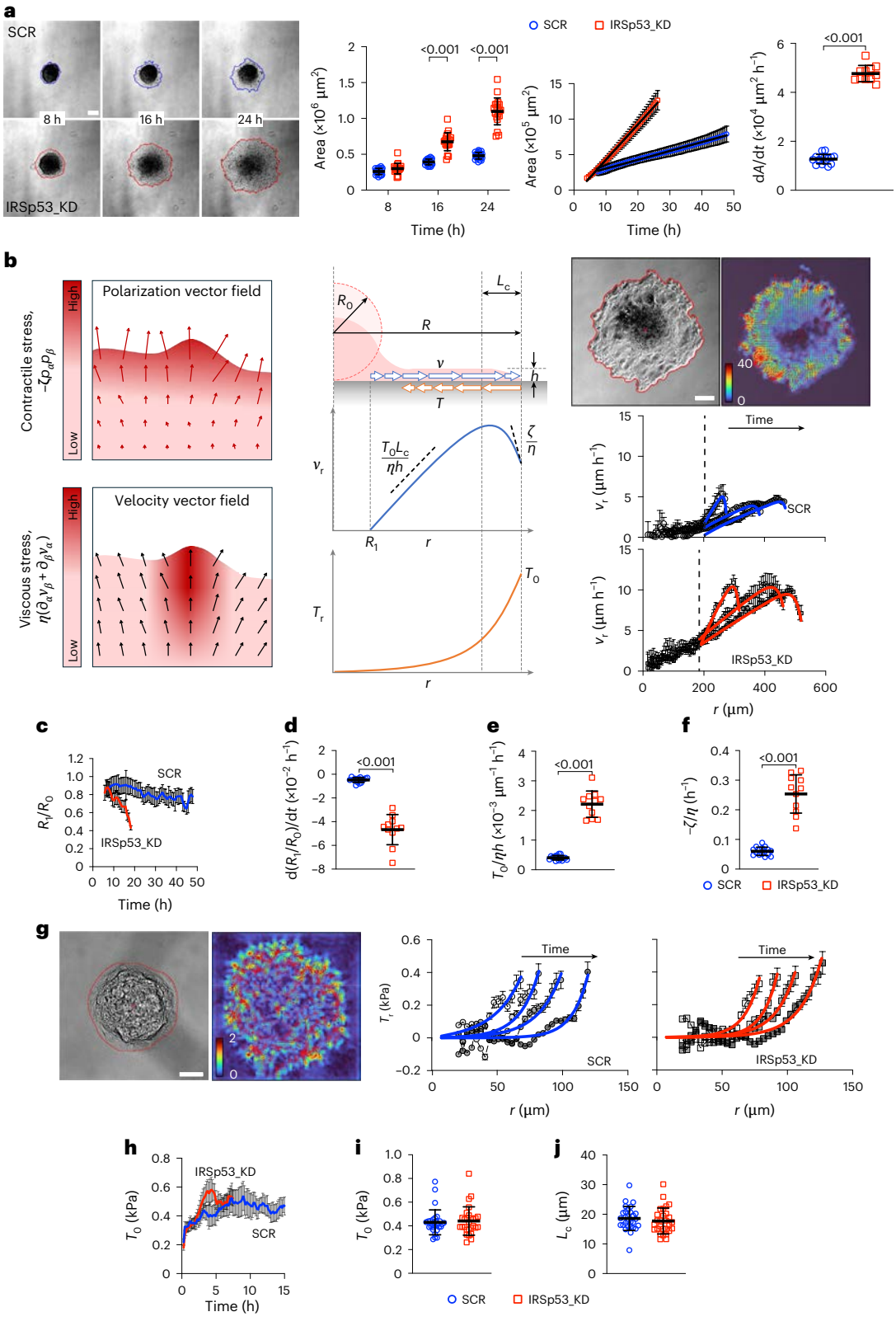

First, we measured the bulk rheological properties of DCIS spheroids using a microfluidic device containing a series of constrictions that impose rapid and repeated deformations[35]. Spheroids of comparable size were flowed through the device under constant pressure, and the transit time through the first constriction—representing the rate-limiting step—was used as an indirect measure of viscous resistance. IRSp53-depleted spheroids traversed the first constriction significantly faster than control spheroids, exhibiting an approximately 50% reduction in transit time (Fig. 3a and Supplementary Video 13). This result indicates reduced viscous dissipation and increased deformability on IRSp53 loss.

To probe the mechanical properties under large, controlled deformations, we next performed atomic force microscopy (AFM) measurements using stiff, tipless cantilevers to compress the spheroids to strains comparable with those experienced in a microfluidic assay[36]. The analysis of force–deformation curves revealed a significant reduction in the apparent surface tension of IRSp53-depleted spheroids compared with controls (Fig. 3b). These findings are consistent with decreased global cohesion and reduced resistance to deformation, supporting a role for IRSp53 in maintaining the bulk mechanical integrity of epithelial aggregates.

We next examined spheroid fusion dynamics, a classical assay to infer the ratio between surface tension and viscosity in viscoelastic droplets[37]. For fluid droplets, the coalescence process is driven by the surface tension σ of the fluid, which tends to minimize the interfacial area, and it is slowed down by the viscosity η, which hinders fluid flow. The initial fusion rate for two droplets of radius R_0 is $\Gamma \simeq \sigma/\eta R_0$ (ref. 37; Fig. 3c). The presence of a non-negligible elastic component in the fluid rheology can prevent complete fusion into a single spherical droplet. In general, the aspect ratio of the final aggregate is expected to be an increasing function of both the ratio between elastic modulus and surface tension and the initial radius R_0 of the coalescing droplets[38]. For both control and IRSp53-devoid spheroids, the fusion rate Γ, obtained by fitting a simple exponential function $a(1-e^{-\Gamma t})$ to the normalized variable $(r/R)^2$, displayed a linear scaling with the inverse of the spheroid radius, as expected based on a viscoelastic droplet model. The amplitude term $a = (r/R)^2_\infty$ is expected to be $\simeq 1$ for complete fusion, whereas for arrested coalescence, $a < 1$. A linear fitting of $\Gamma^{-1}(R_0)$ enabled estimating the ratio σ/η between the effective surface tension and viscosity for both IRSp53 KD ($\sigma/\eta = (1.1 \pm 0.2) \times 10^{-1}$ ms^{-1}) and control spheroids ($\sigma/\eta = (5.7 \pm 1) \times 10^{-2}$ ms^{-1}). In particular, IRSp53-devoid spheroids fused faster (Fig. 3c), leading to significant increase (roughly by a factor of two) of the estimated ratio between surface tension and viscosity. Moreover, although small spheroids fused almost completely ($(r/R)^2_\infty \simeq 1$), for the largest spheroids, we observed arrested coalescence, the deviation of the final configuration from a single sphere being stronger for control spheroids compared with IRSp53 KD spheroids of the same size (Fig. 3c).

Importantly, treating spheroids with EDTA, which sequesters ions crucial for preserving the integrity of cell–cell junctions[39]—whose disruption leads to a decrease in tissue viscosity[40,41]—resulted in a fusion rate increase in the spheroids comparable with that observed with the loss of IRSp53 (Fig. 3d). Moreover, EDTA-treated spheroids displayed complete coalescence ($(r/R)^2_\infty \simeq 1$), whereas this is not the case for control spheroids ($(r/R)^2_\infty \simeq 0.80 \pm 0.05$) (Fig. 3d), suggesting that the treatment also reduces bulk elasticity. In particular, the combined loss of IRSp53 and EDTA treatment further increased the fusion rate and led to the complete fusion of spheroids. These findings support the idea that the loss of IRSp53 changes the biophysical properties of spheroids by decreasing the viscosity and promoting fluidization.

IRSp53 links cell mechanics to collective tension in wetting

In addition to regulating epithelial viscosity, IRSp53 may also influence the effective surface tension (σ) of epithelial collectives, a key parameter governing wetting and fusion dynamics. To distinguish the respective contributions of viscosity and tension to the phenotypes observed on IRSp53 loss, we directly examined how IRSp53 impacts cell–cell adhesion and mechanical tension across multiple scales.

The effective surface tension σ of a cell aggregate represents the ratio between the energetic cost of a deformation leading to a change ΔA in the surface area (cell–matrix contact area) and the area change itself. Within the framework of the differential adhesion hypothesis, σ is determined by the cell–cell adhesion energy per unit area Γ (ref. 42):

$$\sigma \simeq \frac{1}{2}\Gamma. \quad (5)$$

Physically, this equality relies on the simplifying assumption that the cortical tension β_{cc} in portions of the cell membrane corresponding to cell–cell contacts does not differ from the cortical tension β_{cm} associated with cell–matrix contacts[42].

When control and IRSp53-depleted MCF10DCIS.com cells were mixed at equal ratios to form spheroids, IRSp53-depleted cells preferentially localized at the spheroid periphery, whereas control cells occupied the core (Extended Data Fig. 3a). According to the differential adhesion hypothesis[43,44], this sorting behaviour indicates that IRSp53-depleted cells exhibit a lower effective surface tension and reduced intercellular cohesion compared with control cells.

Tissue-scale mechanical properties emerge from the mechanical state of individual cells[1,45]. Therefore, the global changes observed on IRSp53 loss probably reflect its role in modulating individual cell mechanics[14–16,31]. Consequently, we investigated the impact of IRSp53 on cortical tension in both isolated cells and within large 3D aggregates using various approaches.

Using AFM with a tipless cantilever[36], we measured cortical tension in weakly adherent single cells. IRSp53 depletion resulted in an approximately 50% reduction in cortical tension compared with control cells (Extended Data Fig. 3b). A comparable reduction was observed when probing individual cells within 3D spheroids (Extended Data Fig. 3c), indicating that IRSp53 regulates cortical tension both at the single-cell level and in multicellular assemblies.

To determine whether this effect was mediated by actomyosin contractility, we pharmacologically perturbed contractile forces. The inhibition of myosin II with blebbistatin reduced cortical tension in control cells to levels similar to those observed on IRSp53 depletion (Extended Data Fig. 3d). Conversely, the activation of RhoA signalling with CN03 restored cortical tension in IRSp53-depleted cells (Extended Data Fig. 3d), demonstrating that IRSp53 modulates actomyosin-dependent tension.

Consistent with these findings, the modulation of actomyosin contractility altered the spheroid wetting dynamics. Blebbistatin treatment accelerated spheroid spreading and core melting, whereas CN03 treatment reduced spreading and partially rescued the IRSp53 knockdown phenotype (Extended Data Figs. 3e,f and 4a–d and Supplementary Videos 14 and 15). These results establish a direct link between the IRSp53-dependent regulation of cortical tension and 3D spheroids wetting behaviour.

Cortical tension is tightly coupled to the plasma membrane tension[46,47]. We, therefore, measured membrane tension using fluorescence lifetime imaging microscopy (FLIM) with the Flipper-TR probe[48,49]. IRSp53 depletion significantly reduced membrane tension in both sparse cell clusters and confluent monolayers (Fig. 4a), consistent with the observed decrease in cortical tension.

Reduced membrane and cortical tension are expected to impair bleb formation in detached cells[50]. Accordingly, IRSp53-depleted cells displayed markedly reduced blebbing activity following detachment (Fig. 4b and Supplementary Video 16), further supporting a role for IRSp53 in regulating single-cell mechanical properties.

We also performed high-resolution AFM nanomechanical mapping. We observed that the loss of IRSp53 significantly reduces global

https://doi.org/10.1038/s41563-026-02553-2

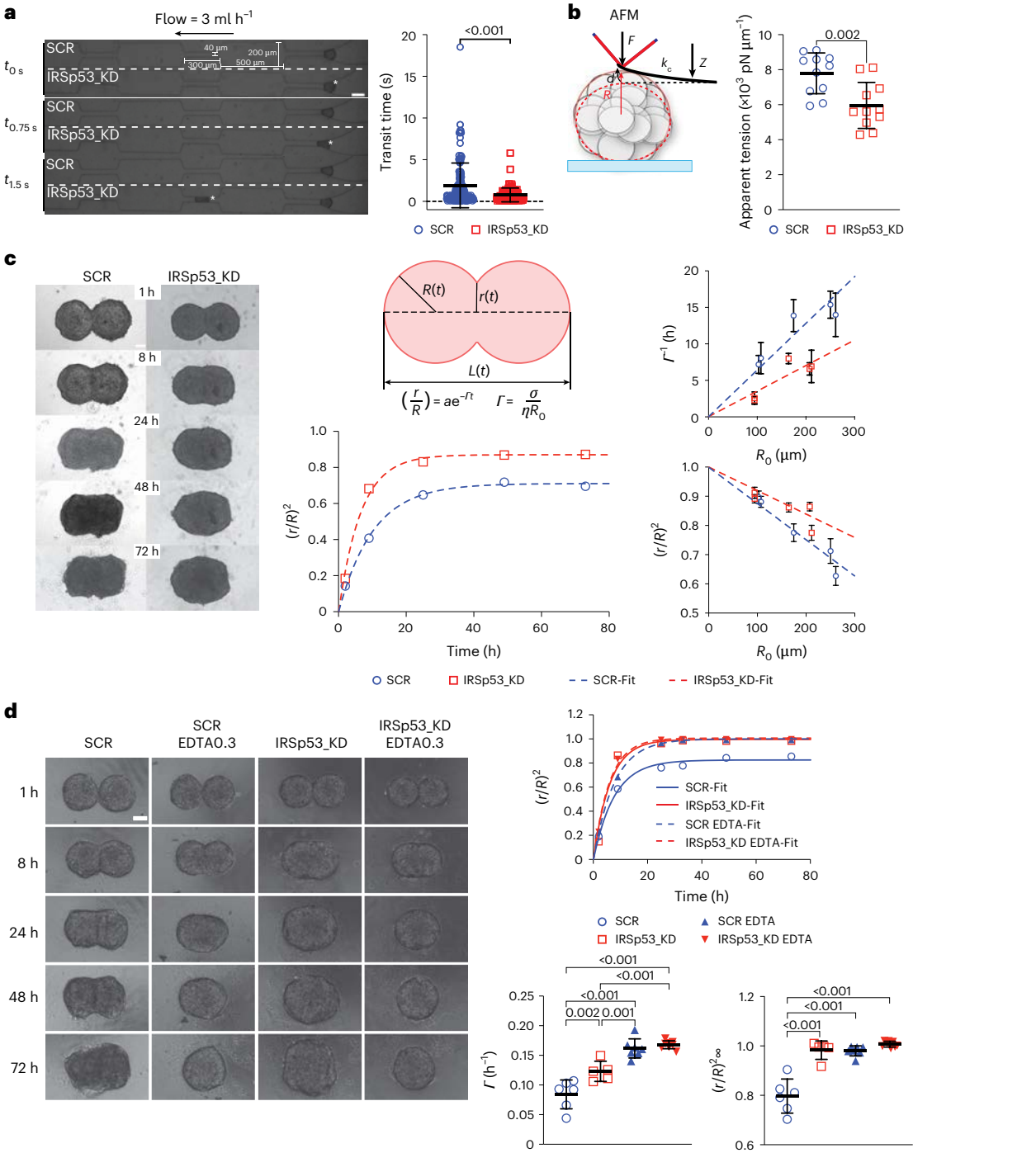

Fig. 3 | IRSp53 controls spheroid viscosity: validation. a, Microfluidic deformation. SCR or IRSp53_KD MCF10DCIS.com spheroids were flowed through a microfluidic device for repetitive deformations[35]. Representative top-view stills show spheroids entering the first three constrictions (Supplementary Video 13); channel dimensions are indicated (height, 190 µm). Scale bar, 100 µm. Right: transit time through the first channel quantified by manual tracking using ImageJ. Mean ± s.d. (n = 261 SCR, 248 IRSp53_KD spheroids; three independent experiments). **b**, AFM probing of spheroids. Left: schematic of a non-adherent spheroid deformed with a tipless AFM cantilever; force is obtained from laser deflection after probe calibration (deflection sensitivity and spring constant). Parameters: applied normal force F, cantilever deflection d, piezo displacement Z, cantilever spring constant k_c and initial spheroid radius R (ref. 36). Right: apparent cortical actomyosin tension of doxycycline-treated SCR and IRSp53_KD spheroids, extracted at Z = 10–15 µm. Mean ± s.d. (n = 11 spheroids; two independent experiments). **c**, Spheroid fusion. SCR and IRSp53_KD cells were used to form spheroids of defined size (500, 2,500 and 5,000 cells). Size-matched spheroid pairs were mixed and fusion followed over time. Left: representative stills (2,500-cell spheroids) at the indicated times. Scale bar, 100 µm. Middle: fusion schematic defining spheroid radius R and neck radius r. Bottom: time evolution of the normalized neck radius squared $(r/R)^2_\infty$ for the shown examples; dashed lines, exponential fits. Right: size dependence of fusion rate Γ (top) and fusion amplitude $(r/R)^2_\infty$ (bottom); dashed lines, linear fits. Mean ± s.d. (n = 9 SCR-500, 7 IRSp53_KD-500; 7 SCR-2500, 9 IRSp53_KD-2500; 7 SCR-5000, 8 IRSp53_KD-5000 spheroid pairs; two independent experiments). **d**, Fusion with reduced adhesion. SCR and IRSp53_KD spheroids were generated using ±0.3 mM of EDTA (EDTA0.3) and fused as above. Left: representative stills. Scale bar, 100 µm. Right: $(r/R)^2_\infty$ versus time with exponential fits (top) and extracted Γ and $(r/R)^2_\infty$ (bottom). Mean ± s.d. (n = 6 SCR, 5 IRSp53_KD, 7 SCR + EDTA, 8 IRSp53_KD + EDTA spheroid pairs; two independent experiments). Statistical tests are listed in Supplementary Table 4; the P values are shown in the graphs.

https://doi.org/10.1038/s41563-026-02553-2

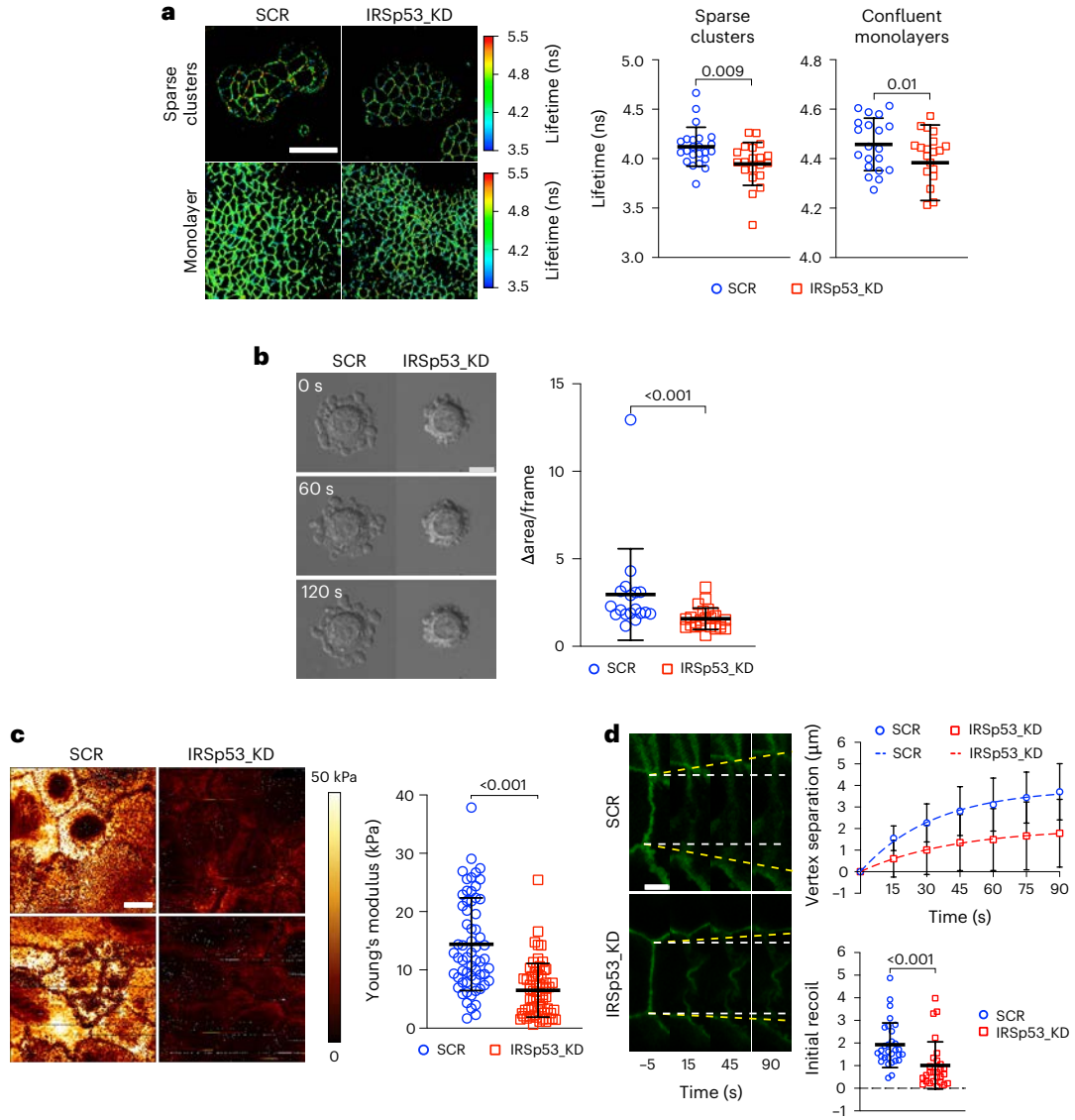

Fig. 4 | IRSp53 governs plasma membrane, cortical and junctional tension. **a**, Live confocal FLIM analysis of SCR and IRSp53_KD MCF10DCIS.com cells seeded to obtain sparse cell clusters or at the jamming density. After 72 h, a Flipper-TR fluorescent membrane tension probe was added to the seeding cells and analysed using confocal microscopy. Left: representative FLIM images with the corresponding calibration bars representing a look-up table of the average Flipper-TR fluorescence lifetime expressed in ns. Scale bar, 10 µm. Right graphs: quantification of in vivo changes in membrane tension of cells clusters or confluent monolayers, respectively. Mean ± s.d. (n = 23 SCR, 20 IRSp53_KD cells in sparse clusters and n = 20 SCR, 19 IRSp53_KD cells in confluent monolayers; two independent experiments). **b**, IRSp53 removal reduces cell blebbing after detachment. Time-lapse microscopy (5 min; time frame, 10 s) of SCR and IRSp53_KD MCF10DCIS.com detached cells 5 min after treatment with trypsin and gentle pipetting (Supplementary Video 16). Left: representative still images at the indicated times. Scale bars, 10 µm. Right: blebbing activity as cell area variation over time (Δarea/frame) (Fiji). Mean ± s.d. (n = 18 SCR, 24 IRSp53_KD cells; two independent experiments). **c**, AFM nanomechanical mapping analysis of SCR and IRSp53_KD MCF10DCIS.com cells seeded and grown to full confluency. Left: representative maps of quantitative imaging to collect Young's modulus maps of regions of cells with an area of 50 × 50 µm^2. Scale bar, 10 µm. Right: Young's modulus quantification. Mean ± s.d. (n = 62 fields; three independent experiments). **d**, Left: GFP–CaaX-positive junctional vertices recoiling after nanoscissor laser ablation at t = 0 in SCR and IRSp53_KD cells (Supplementary Video 17). Recoiling vertices measured as a proxy of junctional tension. White dashed lines, starting positions of vertices; yellow dotted lines, expansion of vertices after laser ablation. Scale bar, 5 µm. Top right graph: initial recoil was measured by the instantaneous rate of vertex separation at t = 0 and computed using the best-fit single exponential curves. Bottom right plot: initial recoil rate. Mean ± s.d., normalized to control (n = 24 SCR, 30 IRSp53_KD; two independent experiments). Statistical tests are listed in Supplementary Table 4; the P values are shown in the graphs.

apical stiffness, as measured by a drop in Young's modulus in confluent monolayers (Fig. 4c).

The reduced intercellular and apical stiffness suggests that junctional tension may also be reduced following the loss of IRSp53. We tested this directly by measuring the rate of vertex recoiling after two-photon-laser-mediated junctional nanoscission. The instantaneous recoil from the cut site indicated that IRSp53 ablation decreased the local junctional tension compared with control cells (Fig. 4d and Supplementary Video 17).

Altogether, these findings demonstrate that IRSp53 coordinates global epithelial tension by regulating the mechanical properties of individual cells, thereby controlling the wetting transition in multicellular spheroids (Supplementary Discussion).

IRSp53 controls viscosity and tension via junction architecture

How does IRSp53 control spheroid viscosity and tension? The viscosity and tensile properties of epithelial collectives depend on the

structural organization of cell–cell junctions, which govern intercellular force transmission and supracellular tension. We, therefore, investigated whether IRSp53 regulates epithelial mechanics by controlling junctional architecture.

We first analysed the cell–cell junction ultrastructure using correlative light and electron microscopy (CLEM) in MCF10DCIS.com spheroids expressing GFP–E-cadherin. In control spheroids, adherens junctions displayed pronounced interdigitated membrane protrusions extending between neighbouring cells (Fig. 5a). By contrast, IRSp53-depleted spheroids exhibited a marked loss of these interdigitations, resulting in smoother and less complex junctional interfaces (Fig. 5a). Focused ion beam–scanning electron microscopy (FIB–SEM) tomography confirmed a strong reduction in intercellular interdigitations in IRSp53-deficient aggregates (Supplementary Videos 18 and 19).

Alterations in junctional architecture were also evident in 2D monolayers. Confocal microscopy of confluent epithelial layers revealed that IRSp53 depletion led to the thinning and disorganization of adherens junctions, as visualized by β-catenin staining, and to a severe reduction in tight junction components, including ZO-1 (Fig. 5b). These structural defects were accompanied by the frequent appearance of enlarged intercellular spaces within IRSp53-depleted monolayers (Extended Data Fig. 5a and Supplementary Videos 20 and 21).

Consistent with weakened junctional organization, IRSp53-depleted cells displayed reduced levels of multiple junctional proteins, including ZO-1, cingulin, N-cadherin and P-cadherin (Extended Data Fig. 5b). A modest but significant reduction in cell surface E-cadherin was also detected by fluorescence-activated cell sorting and confocal microscopy (Extended Data Fig. 5c,d). In particular, E-cadherin internalization rates were unchanged (Extended Data Fig. 5e), suggesting that impaired recycling or junctional stabilization, rather than increased endocytosis, underlies the reduced surface levels.

Epithelial cells after prolonged culture as 2D monolayers have been shown to spontaneously self-organized to generate the formation of dynamics dome-like structures on solid growth supports. Dome formation requires active polarized fluid transport and the establishment of tight supracellular barrier and tensile junctional structures[51], which were compromised in IRSp53-silenced monolayers. Consistently, control monolayers formed dynamically expanding and contracting domes, which were instead completely absent after the silencing of IRSp53 (Extended Data Fig. 5f,g and Supplementary Videos 22 and 23).

The altered junctional architecture may also compromise the junctional tensile state and prevent the formation of supracellular tensile cytoskeletal structures. In line with this, the confocal analysis of MCF10DCIS.com monolayers revealed that IRSp53 removal impeded the formation of force-transmitting actin cables that in control cells extend through the cell adhesive junction across multiple cells (Fig. 5c). In particular, the formation of a supracellular actin cable in IRSp53-silenced cells could be nearly completely rescued by increasing actomyosin contractility by the treatment of monolayers with the RhoA-activator CN03 (Fig. 5c). Conversely, the inhibition of actomyosin contractility by the addition of blebbistatin to control monolayers disrupted the formation of a supracellular actin cable phenocopying the loss of IRSp53 (Fig. 5c). Of note, although blebbistatin treatment induced a drastic loss of tight junctions in SCR monolayer, probably due to its inhibitory activity on actomyosin motor, the architecture of adherens junction was preserved (Extended Data Fig. 6a); on the other end, CN03 could not rescue both tight junction formation and adherens junction architecture in IRSp53 KD monolayer (Extended Data Fig. 6b). Altogether, these data show that IRSp53 does not directly alter actomyosin contractility but probably impinges on forces transmission mechanisms.

Thus, IRSp53 controls epithelial collective viscosity and surface tension by regulating cell junction structure and interfacial tension, reinforcing the notion that this protein is crucial in linking global tissue mechanics to the mechanical properties of individual cells.

Low and delocalized IRSp53 in DCIS predicts poor survival

Our findings suggest IRSp53 as a key regulator of the viscoelastic state of epithelial collectives, linking molecular-scale adhesion dynamics to large-scale phase transitions relevant to tumour progression. Reduction in IRSp53 levels induces a weakening of cell junction, resulting in decreased supracellular tension and increased fluidification in cell collectives. Thus, IRSp53 controls the mechanical properties of both collective and single cells, increasingly recognized as hallmarks of cancer[1–3].

If this is the case, depletion or mislocalization of this protein might have an impact on tumour progression. To address this point, we interrogated public tumour data banks and we found that low IRSp53 protein levels correlate with reduced overall survival in breast cancer (https://kmplot.com/ and ref. 52; Extended Data Fig. 7a). Additionally, we analysed IRSp53 localization in a tissue microarray (TMA) comprising a retrospective consecutive cohort of 1,631 female patients, from the European Institute of Oncology in Milan[53,54], with complete clinicopathological follow-up. The results highlight an aberrant localization of IRSp53 during DCIS progression, compared with normal breast epithelia, which correlate with worse clinical outcomes (Extended Data Fig. 7b).

These results emphasize the potential clinical relevance of IRSp53 in tumour progression.

IRSp53 interact with AFD to control viscoelasticity

IRSp53 is a multidomain protein comprising an N-terminal I-BAR domain, a CRIB–proline-rich region, an SH3 domain and a C-terminal PDZ-binding motif[14,16,55]. To identify molecular partners linking IRSp53 to junctional mechanics, we analysed the IRSp53 proximity interactome previously generated using SILAC-based proteomics and BirA-mediated proximity labelling[21]. Through RNAi screening in a 3D spheroid spreading assay, we tested multiple candidate genes to determine which interactors of IRSp53 could mimic its loss-of-function phenotypes. AFD emerged as the only effective candidate. AFD is a junctional protein essential during development in mice, *Drosophila* and *Caenorhabditis elegans*[27,28,30]; it has been shown to specifically influence the epithelial cortical tension[29] and the epithelial polarity program as IRSp53 (ref. 26). This suggests that AFD may function in a similar pathway or as a key partner in regulating cell junctions and collective cell movement, making it a critical player in maintaining tissue integrity alongside IRSp53. Consistently, AFD ablation phenocopied IRSp53 loss during 3D spheroid wetting (Fig. 6a, Extended Data Fig. 8a,b and Supplementary Video 24).

To confirm a physical interaction, we performed co-immuno precipitation experiments in HEK293T cells. AFD selectively associated with an IRSp53 SH3-defective mutant (W413G), but not with wild-type (WT) IRSp53 (Fig. 6b). IRSp53 is known to adopt a closed, autoinhibited conformation in which the CRIB–PR region binds the SH3 domain; the cooperative binding of Cdc42 and SH3-interacting partners induces an open, active conformation[55]. These results suggest that AFD preferentially interacts with the open conformation of IRSp53.

In vitro pull-down assays using purified IRSp53 fragments further demonstrated that AFD binding requires the C-terminal region of IRSp53 but not the SH3 domain (Extended Data Fig. 8c). Structural modelling using AlphaFold3 predicted a canonical interaction between the PDZ-binding motif of IRSp53 (VSTV[21]) and the PDZ domain of AFD (Extended Data Fig. 8d), which was confirmed by direct binding assays using purified proteins (Fig. 6c).

AFD has been shown to regulate epithelial cortical tension by controlling the apical actomyosin network[29]. We, therefore, tested whether IRSp53 and AFD converge functionally on epithelial mechanics. Two-photon laser ablation of the apical cortex revealed that the

https://doi.org/10.1038/s41563-026-02553-2

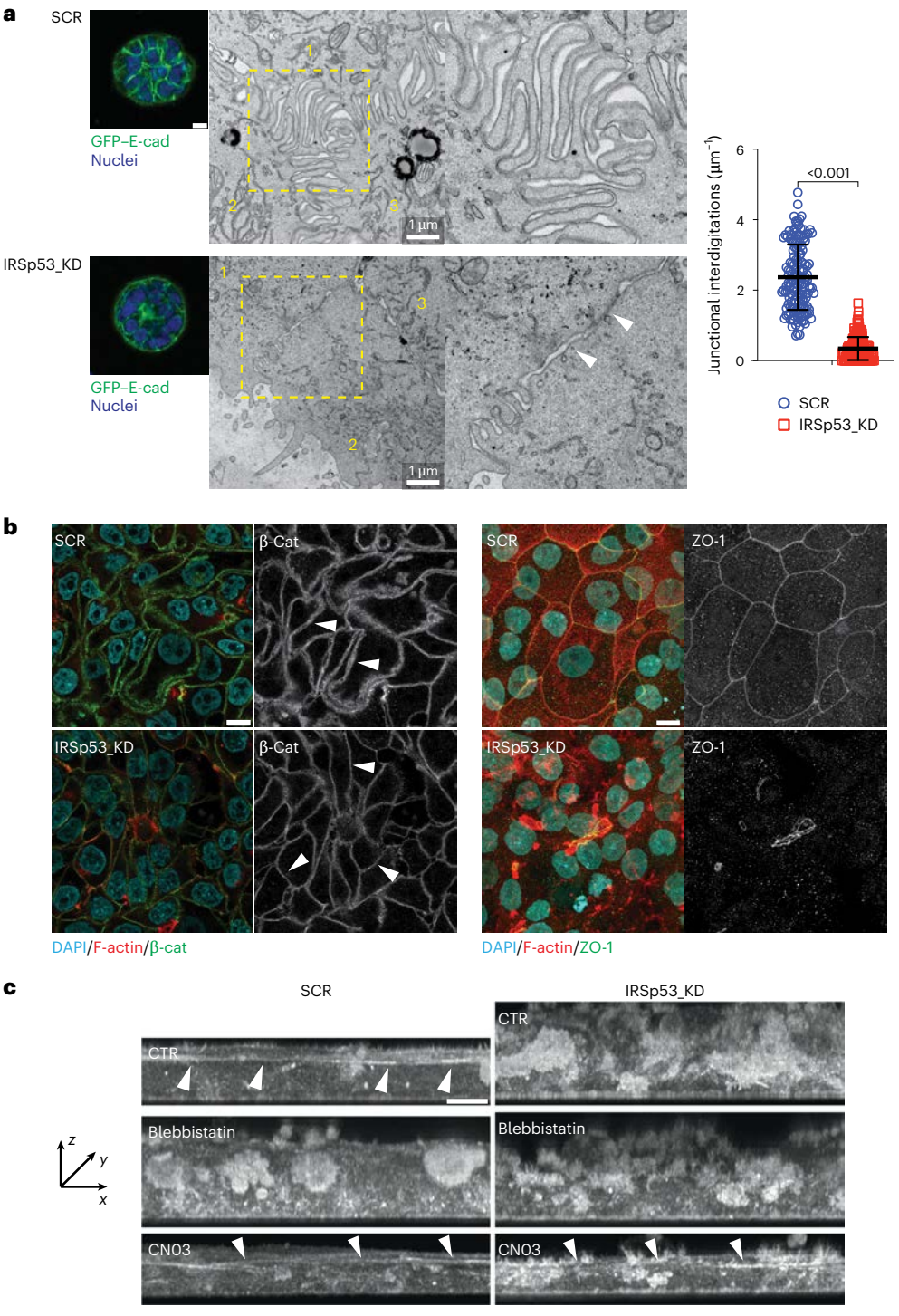

Fig. 5 | IRSp53 regulates viscosity and surface tension by shaping junction architecture. a, SCR or IRSp53_KD MCF10DCIS.com cells, expressing GFP–E-cadherin, were plated as single cells on Matrigel-coated gridded coverslips and cultured in a medium containing 2% Matrigel. Resulting spheroids were stained with NucBlue Live ReadyProbes (nuclei, blue), located on the grid by confocal microscopy. Scale bar, 10 µm. Thereafter, they were processed for electron microscopy; the corresponding electron microscopy images are shown (numbers mark individual cells). Insets (2×) correspond to dashed boxes. Arrowheads highlight reduced plasma-membrane interdigitations at cell–cell junctions in IRSp53_KD spheroids. Right: junctional interdigitation quantified as interdigitation (µm). Mean ± s.d. (n = 152 fields/4 SCR spheroids, 204 fields/4 IRSp53_KD spheroids; three independent experiments), scored from serial Z sections. FIB–SEM tomography was performed on the same spheroids (Supplementary Videos 18 and 19). **b**, Left: confocal sections (5 µm above the bottom surface) of doxycycline-treated SCR and IRSp53_KD cells seeded at the jamming density and fixed 96 h post-seeding, stained for β-catenin (green), F-actin (TRITC–phalloidin, red) and DAPI (blue). Arrowheads indicate altered/thinner junctional architecture in IRSp53_KD. Scale bar, 10 µm. Right: ZO-1 staining in analogous samples fixed at 96 h; confocal Z stacks acquired with 0.5-µm steps and displayed as maximum projections (ZO-1 shown). Scale bar, 10 µm. **c**, Jammed SCR and IRSp53_KD monolayers were treated 16 h before fixation with dimethyl sulfoxide (DMSO; CTR), 5 µM of blebbistatin or 10 µg ml^{-1} of CN03, fixed at 96 h and stained for F-actin (TRITC–phalloidin; β-catenin/ZO-1 and DAPI are not shown). Confocal Z stacks (0.5-µm steps) were resliced along the y axis in ImageJ; the maximum projections of the F-actin channel are shown. Arrowheads (SCR CTR, SCR CN03 and IRSp53_KD CN03) indicate a supracellular actin cable. Scale bar, 10 µm. Statistical tests are listed in Supplementary Table 4; the P values are shown in the graphs.

https://doi.org/10.1038/s41563-026-02553-2

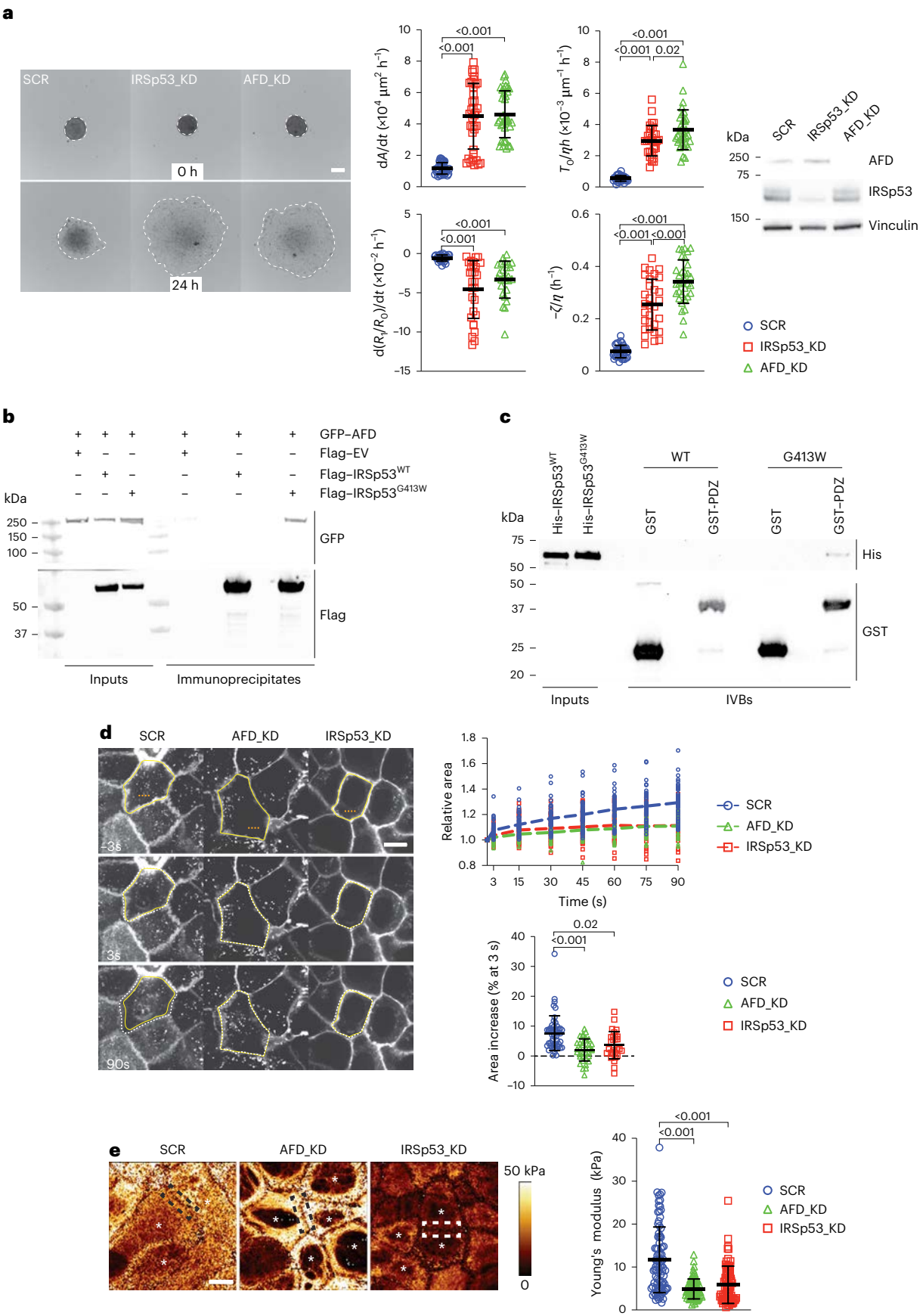

Fig. 6 | IRSp53 interacts with AFD to control viscoelasticity. a, Time lapse of SCR, IRSp53_KD or AFD-silenced (AFD_KD) MCF10DCIS.com spheroids seeded on fibronectin-coated six-well plates (Supplementary Video 24). Top left: representative still images at the indicated times. Scale bar, 200 µm. Top right: immunoblotting for IRSp53 and AFD (antibodies indicated). Bottom: spreading parameters from image segmentation and PIV: rate of spreading dA/dt, rate of core melting $d(R_1/R_0)/dt$, A, and B. Mean ± s.d. from three independent experiments (dA/dt: $n = 34$ SCR, 37 IRSp53_KD, 36 AFD_KD spheroids; $d(R_1/R_0)/dt$: $n = 26$ SCR, 29 IRSp53_KD, 26 AFD_KD spheroids; A and B: $n = 34$ SCR, 31 IRSp53_KD, 33 AFD_KD spheroids). **b**, IRSp53–AFD interaction is enhanced by SH3 loss of function. Co-immunoprecipitation from 293T cells transfected with the indicated constructs: 4 mg of lysate immunoprecipitated with anti-Flag. Inputs (20 µg) and immunoprecipitates were immunoblotted with the indicated antibodies. **c**, Direct binding via the AFD PDZ domain. Purified GST or GST–AFD PDZ (0.5 µM) was incubated with purified His–IRSp53 (WT or G413W; 0.75 µM). Inputs and in vitro binding samples were resolved by sodium dodecyl sulfate–polyacrylamide gel electrophoresis and immunoblotted with the indicated antibodies. **d**, IRSp53 loss reduces cortical tension. SCR, AFD_KD and IRSp53_KD monolayers expressing mCherry–CaaX were subjected to terminal web laser ablation (Supplementary Video 25). Left: representative ablations; the dotted orange line indicates the ablation site; cell contour at $t = 0$ (solid yellow) and later times (dashed white). Scale bar, 10 µm. Top right: normalized apical area over time after ablation (symbols, single cells; dashed lines, cell-type average; areas normalized to 1 at $t = 0$). Bottom right: initial area expansion quantified as relative area change between $t = 0$ and $t = 3$ s (ref. 29). Mean ± s.d. ($n = 50$ SCR, 36 AFD_KD, 29 IRSp53_KD cells; two independent experiments). **e**, AFM nanomechanical mapping. SCR, AFD_KD and IRSp53_KD cells grown to full confluency were analysed by quantitative imaging to generate Young's modulus maps (regions: 50×50 µm^2). Left: representative maps. White asterisks mark nuclear regions; dotted boxes highlight peri-junctional regions (black, SCR/AFD_KD; white, IRSp53_KD). Scale bar, 10 µm. Right: Young's modulus quantification. Mean ± s.d. ($n = 89$ SCR, 79 AFD_KD, 73 fields; three independent experiments). Statistical tests are listed in Supplementary Table 4; the P values are shown in the graphs.

depletion of either IRSp53 or AFD reduced apical tension compared with control cells (Fig. 6d and Supplementary Video 25). These results indicate that both proteins contribute to the maintenance of cortical tension.

Consistent with this conclusion, AFM-based nanomechanical mapping of confluent monolayers showed that AFD depletion reduced global apical stiffness in the nuclear region to an extent comparable with IRSp53 loss (Fig. 6e). In particular, unlike IRSp53 ablation, AFD depletion did not significantly soften the peri-junctional regions, suggesting that the two proteins share overlapping but non-identical mechanical functions.

Importantly, IRSp53 depletion caused a pronounced delocalization of AFD from cell–cell junctions without altering the total AFD protein levels (Extended Data Fig. 8e), indicating that IRSp53 is required for proper AFD junctional localization and function.

Together, these findings identify AFD as a key functional interactor of IRSp53 that links junctional architecture to epithelial viscoelasticity. By regulating AFD localization and activity at cell–cell junctions, IRSp53 integrates molecular-scale interactions with collective-scale mechanical behaviour.

Outlook

This study identifies IRSp53 and its functional partner AFD as central regulators of the viscoelastic properties of epithelial collectives, providing a molecular framework for understanding solid-to-fluid transitions that are critical during tumour progression (Extended Data Fig. 9). We show that IRSp53 regulates junctional architecture, supracellular tension and intercellular cohesion, thereby controlling epithelial viscosity, fluidification and active wetting. Loss of IRSp53 weakens junctional organization, reduces force transmission and promotes local cellular rearrangements, driving a transition from a solid-like to a fluid-like collective state.

At the molecular level, IRSp53 interacts with AFD to coordinate cortical and junctional mechanics. AFD, a known regulator of epithelial polarity and cortical tension, cooperates with IRSp53 to maintain the structural and mechanical integrity of cell–cell junctions. Through this interaction, IRSp53 links membrane–cytoskeleton coupling at the single-cell level to emergent tissue-scale mechanical behaviour, integrating cellular tension, junctional architecture and collective dynamics.

These findings contribute to a growing understanding of how molecular regulators of cytoskeletal organization shape tissue mechanics in cancer. By revealing how the IRSp53-dependent control of viscosity and tension governs epithelial fluidification, this work highlights solid-to-fluid transitions as actionable biophysical processes during tumour progression. Consistent with this view, an analysis of patient samples shows that the reduced expression and aberrant localization of IRSp53 correlate with poor clinical outcome in breast cancer, underscoring the pathological relevance of IRSp53-regulated tissue mechanics. Future studies will be needed to define how IRSp53–AFD-dependent mechanical regulation interfaces with other biophysical and biological processes, including ECM remodelling, stromal interactions and immune infiltration. Extending this framework to other epithelial tissues and disease contexts may reveal broader principles by which junctional mechanics and tissue viscoelasticity govern morphogenesis, regeneration and cancer invasion.

Online content

Any methods, additional references, Nature Portfolio reporting summaries, source data, extended data, supplementary information, acknowledgements, peer review information; details of author contributions and competing interests; and statements of data and code availability are available at https://doi.org/10.1038/s41563-026-02553-2.

References

1. Ayad, N. M. E., Kaushik, S. & Weaver, V. M. Tissue mechanics, an important regulator of development and disease. *Philos. Trans. R. Soc. Lond. B Biol. Sci.* **374**, 20180215 (2019).
2. Massey, A. et al. Mechanical properties of human tumour tissues and their implications for cancer development. *Nat. Rev. Phys.* **6**, 269–282 (2024).
3. Nia, H. T., Munn, L. L. & Jain, R. K. Physical traits of cancer. *Science* **370**, eaaz0868 (2020).
4. Bi, D., Lopez, J. H., Schwarz, J. M. & Manning, M. L. A density-independent rigidity transition in biological tissues. *Nat. Phys.* **11**, 1074–1079 (2015).
5. Blauth, E., Kubitschke, H., Gottheil, P., Grosser, S. & Käs, J. A. Jamming in embryogenesis and cancer progression. *Front. Phys.* **9**, 666709 (2021).
6. Douezan, S. et al. Spreading dynamics and wetting transition of cellular aggregates. *Proc. Natl Acad. Sci. USA* **108**, 7315–7320 (2011).
7. Malinverno, C. et al. Endocytic reawakening of motility in jammed epithelia. *Nat. Mater.* **16**, 587–596 (2017).
8. Mongera, A. et al. A fluid-to-solid jamming transition underlies vertebrate body axis elongation. *Nature* **561**, 401–405 (2018).
9. Perez-Gonzalez, C. et al. Active wetting of epithelial tissues. *Nat. Phys.* **15**, 79–88 (2019).
10. Pinheiro, D. & Mitchel, J. Pulling the strings on solid-to-liquid phase transitions in cell collectives. *Curr. Opin. Cell Biol.* **86**, 102310 (2024).
11. Gottheil, P. et al. State of cell unjamming correlates with distant metastasis in cancer patients. *Phys. Rev.* **13**, 031003 (2023).
12. Palamidessi, A. et al. Unjamming overcomes kinetic and proliferation arrest in terminally differentiated cells and promotes collective motility of carcinoma. *Nat. Mater.* **18**, 1252–1263 (2019).

13. Beaune, G. et al. Reentrant wetting transition in the spreading of cellular aggregates. *Soft Matter* **13**, 8474–8482 (2017).
14. Disanza, A. et al. CDC42 switches IRSp53 from inhibition of actin growth to elongation by clustering of VASP. *EMBO J.* **32**, 2735–2750 (2013).
15. Disanza, A. et al. Regulation of cell shape by Cdc42 is mediated by the synergic actin-bundling activity of the Eps8-IRSp53 complex. *Nat. Cell Biol.* **8**, 1337–1347 (2006).
16. Scita, G., Confalonieri, S., Lappalainen, P. & Suetsugu, S. IRSp53: crossing the road of membrane and actin dynamics in the formation of membrane protrusions. *Trends Cell Biol.* **18**, 52–60 (2008).
17. Goh, W. I. et al. mDia1 and WAVE2 proteins interact directly with IRSp53 in filopodia and are involved in filopodium formation. *J. Biol. Chem.* **287**, 4702–4714 (2012).
18. Takenawa, T. & Suetsugu, S. The WASP-WAVE protein network: connecting the membrane to the cytoskeleton. *Nat. Rev. Mol. Cell Biol.* **8**, 37–48 (2007).
19. Li, J. X. H., Tang, V. W., Boateng, K. A. & Brieher, W. M. Cadherin puncta are interdigitated dynamic actin protrusions necessary for stable cadherin adhesion. *Proc. Natl Acad. Sci. USA* **118**, e2023510118 (2021).
20. Li, J. X. H., Tang, V. W. & Brieher, W. M. Actin protrusions push at apical junctions to maintain E-cadherin adhesion. *Proc. Natl Acad. Sci. USA* **117**, 432–438 (2020).
21. Bisi, S. et al. IRSp53 controls plasma membrane shape and polarized transport at the nascent lumen in epithelial tubules. *Nat. Commun.* **11**, 3516 (2020).
22. Cohen, D., Fernandez, D., Lazaro-Dieguez, F. & Musch, A. The serine/threonine kinase Par1b regulates epithelial lumen polarity via IRSp53-mediated cell-ECM signaling. *J. Cell Biol.* **192**, 525–540 (2011).
23. Massari, S. et al. LIN7 mediates the recruitment of IRSp53 to tight junctions. *Traffic* **10**, 246–257 (2009).
24. Moreno-Layseca, P. et al. Cargo-specific recruitment in clathrin- and dynamin-independent endocytosis. *Nat. Cell Biol.* **23**, 1073–1084 (2021).
25. Miller, F. R. Xenograft models of premalignant breast disease. *J Mammary Gland Biol. Neoplasia* **5**, 379–391 (2000).
26. Carminati, M. et al. Concomitant binding of Afadin to LGN and F-actin directs planar spindle orientation. *Nat. Struct. Mol. Biol.* **23**, 155–163 (2016).
27. Hall, A. E., Klompstra, D. & Nance, J. *C. elegans* Afadin is required for epidermal morphogenesis and functionally interfaces with the cadherin-catenin complex and RhoGAP PAC-1/ARHGAP21. *Dev. Biol.* **511**, 12–25 (2024).
28. Ikeda, W. et al. Afadin: a key molecule essential for structural organization of cell-cell junctions of polarized epithelia during embryogenesis. *J. Cell Biol.* **146**, 1117–1132 (1999).
29. Mangeol, P. et al. The zonula adherens matura redefines the apical junction of intestinal epithelia. *Proc. Natl Acad. Sci. USA* **121**, e2316722121 (2024).
30. Sawyer, J. K., Harris, N. J., Slep, K. C., Gaul, U. & Peifer, M. The *Drosophila* Afadin homologue Canoe regulates linkage of the actin cytoskeleton to adherens junctions during apical constriction. *J. Cell Biol.* **186**, 57–73 (2009).
31. Prevost, C. et al. IRSp53 senses negative membrane curvature and phase separates along membrane tubules. *Nat. Commun.* **6**, 8529 (2015).
32. Ilina, O. et al. Cell-cell adhesion and 3D matrix confinement determine jamming transitions in breast cancer invasion. *Nat. Cell Biol.* **22**, 1103–1115 (2020).
33. Giavazzi, F., Malinverno, C., Scita, G. & Cerbino, R. Tracking-free determination of single-cell displacements and division rates in confluent monolayers. *Front. Phys.* **6**, 120 (2018).
34. Cronin, N. M. & DeMali, K. A. Dynamics of the actin cytoskeleton at adhesion complexes. *Biology* **11**, 52 (2021).
35. Makkieh, M. et al. Brillouin microscopy of breast tumor spheroids on-a-chip: mechanical and transcriptional responses to microfluidic-induced rapid deformations. *Adv. Sci.* **13**, e13153 (2025).
36. Cartagena-Rivera, A. X., Logue, J. S., Waterman, C. M. & Chadwick, R. S. Actomyosin cortical mechanical properties in nonadherent cells determined by atomic force microscopy. *Biophys. J.* **110**, 2528–2539 (2016).
37. Grosser, S. et al. Cell and nucleus shape as an indicator of tissue fluidity in carcinoma. *Phys. Rev.* **11**, 011033 (2021).
38. Pawar, A. B., Caggioni, M., Hartel, R. W. & Spicer, P. T. Arrested coalescence of viscoelastic droplets with internal microstructure. *Faraday Discuss.* **158**, 341–350 (2012).
39. Meng, W. & Takeichi, M. Adherens junction: molecular architecture and regulation. *Cold Spring Harb. Perspect. Biol.* **1**, a002899 (2009).
40. Cartagena-Rivera, A. X., Van Itallie, C. M., Anderson, J. M. & Chadwick, R. S. Apical surface supracellular mechanical properties in polarized epithelium using noninvasive acoustic force spectroscopy. *Nat. Commun.* **8**, 1030 (2017).
41. David, R. et al. Tissue cohesion and the mechanics of cell rearrangement. *Development* **141**, 3672–3682 (2014).
42. Manning, M. L., Foty, R. A., Steinberg, M. S. & Schoetz, E. M. Coaction of intercellular adhesion and cortical tension specifies tissue surface tension. *Proc. Natl Acad. Sci. USA* **107**, 12517–12522 (2010).
43. Steinberg, M. S. Reconstruction of tissues by dissociated cells. Some morphogenetic tissue movements and the sorting out of embryonic cells may have a common explanation. *Science* **141**, 401–408 (1963).
44. Wang, S., Matsumoto, K., Lish, S. R., Cartagena-Rivera, A. X. & Yamada, K. M. Budding epithelial morphogenesis driven by cell-matrix versus cell-cell adhesion. *Cell* **184**, 3702–3716.e3730 (2021).
45. Kumar, S. & Weaver, V. M. Mechanics, malignancy, and metastasis: the force journey of a tumor cell. *Cancer Metastasis Rev.* **28**, 113–127 (2009).
46. Chugh, P. et al. Actin cortex architecture regulates cell surface tension. *Nat. Cell Biol.* **19**, 689–697 (2017).
47. Koster, D. V. & Mayor, S. Cortical actin and the plasma membrane: inextricably intertwined. *Curr. Opin. Cell Biol.* **38**, 81–89 (2016).
48. Dal Molin, M. et al. Fluorescent flippers for mechanosensitive membrane probes. *J. Am. Chem. Soc.* **137**, 568–571 (2015).
49. Pandzic, E., Whan, R. & Macmillan, A. Rapid FLIM measurement of membrane tension probe Flipper-TR. *Methods Mol. Biol.* **2402**, 257–283 (2022).
50. Weems, A. D. et al. Blebs promote cell survival by assembling oncogenic signalling hubs. *Nature* **615**, 517–525 (2023).
51. Lechner, J., Hekl, D., Gatt, H., Voelp, M. & Seppi, T. Monitoring of the dynamics of epithelial dome formation using a novel culture chamber for long-term continuous live-cell imaging. *Methods Mol. Biol.* **763**, 169–178 (2011).
52. Győrffy, B. Survival analysis across the entire transcriptome identifies biomarkers with the highest prognostic power in breast cancer. *Comput. Struct. Biotechnol. J.* **19**, 4101–4109 (2021).
53. Salemme, V. et al. p140Cap inhibits β-catenin in the breast cancer stem cell compartment instructing a protective anti-tumor immune response. *Nat. Commun.* **14**, 2350 (2023).
54. Schiano Lomoriello, I. et al. A self-sustaining endocytic-based loop promotes breast cancer plasticity leading to aggressiveness and pro-metastatic behavior. *Nat. Commun.* **11**, 3020 (2020).
55. Kast, D. J. et al. Mechanism of IRSp53 inhibition and combinatorial activation by Cdc42 and downstream effectors. *Nat. Struct. Mol. Biol.* **21**, 413–422 (2014).

[1]IFOM ETS, the AIRC Institute of Molecular Oncology, Milan, Italy. [2]Department of Medical Biotechnology and Translational Medicine, University of Milan, Segrate, Italy. [3]Section on Mechanobiology, National Institute of Biomedical Imaging and Bioengineering, National Institutes of Health, Bethesda, MD, USA. [4]Department of Cellular Biophysics, Max Planck Institute for Medical Research, Heidelberg, Germany. [5]Department of Oncology and Haemato-Oncology, University of Milan, Milan, Italy. [6]European Institute of Oncology (IEO) IRCCS, Milan, Italy. [7]Carl Zeiss Microscopy GmbH, Oberkochen, Germany. [8]Radboud University, Nijmegen, The Netherlands. [9]Cellular Biomechanics, University of Bayreuth, Bayreuth, Germany. [10]Present address: Fondazione Human Technopole, Milan, Italy. [11]Present address: Unità Operativa Multizonale di Anatomia Patologica APSS, Trento, Italy. [12]Present address: Centre for Medical Sciences—CISMed University of Trento, Trento, Italy. [13]Present address: Dipartimento di Medicina Molecolare e Biotecnologie Mediche, Università degli Studi di Napoli Federico II, Naples, Italy. [14]These authors jointly supervised this work: Alexander X. Cartagena-Rivera, Fabio Giavazzi, Giorgio Scita, Andrea Disanza. ✉e-mail: giorgio.scita@ifom.eu

Methods

Set of standard methods and reagents

A set of standard methods and reagents are included in the Supplementary Information. This research complies with all relevant ethical regulations. All animal experiments were approved by the institutional organism for animal welfare and ethical approach to animals in experimental procedures (Cogentech OPBA). All animal studies were conducted with the approval of the Italian Ministry of Health (1192/2020-PR) and were performed in accordance with Italian law (D.lgs. 26/2014), which enforces Dir. 2010/63/EU (Directive 2010/63/EU of the European Parliament and of the Council of 22 September 2010 on the protection of animals used for scientific purposes). For the analysis of TMA obtained from a consecutive cohort of female breast cancer patients, all patients provided written informed consent and underwent surgical procedures at the European Institute of Oncology, Milan, from 1997 to 2000.

Antibodies and DNA constructs

The complete list of used antibodies and DNA constructs are reported in Supplementary Tables 2 and 3.

Collective motility (wound healing)

SCR and IRSp53_KD cells were seeded in six-well plate (1.5×10^6 cells per well) in complete medium with 1 μg ml^{-1} of doxycycline. The day after, monolayer was scratched with a pipette tip and carefully washed with 3× phosphate-buffered saline (PBS) to remove cells and create a cell-free wound area. The closure of the wound was monitored by time-lapse imaging with a Leica TIRF inverted microscope (wide-field acquisition only) with a ×10 objective every 10 min for 24 h, at 37 °C in a humidified atmosphere with 5% CO_2.

The percentage of area covered by cells over time was calculated using a custom Fiji (ImageJ2, v. 2.16.0/1.54p) and MATLAB (version R2019a) code. The area covered over time was fitted with two straight lines (https://github.com/aganse/MultiRegressLines.matlab/blob/master/regress2lines.m) and the slope of the second line was used to estimate the maximum rate of coverage, after a lag phase. On the cell layers identified, velocity fields were extracted with PIV using the MATLAB mpiv toolbox (https://www.oceanwave.jp/softwares/mpiv/index.php), with an interrogation window of 60×60 μm^2 and a 25% of overlap and a time interval of 10 min between two consecutive frames. The correlation length (L_{corr}) was estimated by fitting the normalized velocity spatial correlation function, along the radius r, with an exponential function $e^{-r/L_{corr}}$.

Directionality index was obtained by manually tracking the leader cells at the migrating front with Manual Tracking plug-in from Fiji and analysing the obtained trajectories with the Chemotaxis Tool plug-in.

Single-cell tracking was carried out by first segmenting the fluorescent nuclei with StarDist (Fiji)[56] and then tracking the labelled nuclei with TrackMate (Fiji)[57,58]. Further processing for the selection of trajectories and the quantification of their straightness was carried out with MATLAB. Only trajectories lasting for at least 15 consecutive frames have been considered for the evaluation of the straightness parameter, defined as the ratio between the end-to-end distance and the total trajectory length. Single-cell tracking was stopped before the wound was completely closed.

Unjamming-to-jamming transition

SCR (H2B-GFP-labelled) and IRSp53_KD (H2B-mCherry-labelled) cells were seeded in confluent conditions (near the jamming density) in a 12-well plate (6×10^5 cells per well) in complete medium with 1 μg ml^{-1} of doxycycline. The day after, transition from the unjamming (fluid-like) to complete jamming (solid-like) state was monitored by time-lapse imaging using an Olympus ScanR inverted microscope with a ×10 objective every 10 min for 72 h, at 37 °C in a humidified atmosphere with 5% CO_2.

Maps of the instantaneous cellular velocities were obtained by analysing time-lapse phase-contrast movies of cell monolayers with PIV using a custom MATLAB script. The interrogation windows were typically 64 or 128 pixels (44.9 or 52.3 μm) on a side, with 50% overlap between adjacent windows. For a given monolayer, time-lapse images from eight different fields of view were simultaneously collected.

PIV analysis quantifies the speed and direction of cell flow within each interrogation window. From the velocity map, we computed the instantaneous velocity of the centre of mass as the average velocity $v_{CM}(t) = \langle v_i(t) \rangle_i$, where $v_i(t)$ is the instantaneous velocity at time t in the ith interrogation window and $\langle \cdot \rangle_i$ denotes the average over all the interrogation windows. The root mean square velocity was then quantified as $v_{r.m.s.}(t) = \sqrt{\langle |v_i(t) - v_{CM}(t)|^2 \rangle_i}$. The time evolution of $v_{r.m.s.}$ was calculated for each single field of view. Results were then averaged, at each time point, over all fields of view of the same cell type.

Single-cell tracking was carried out for comparison by first segmenting the fluorescent nuclei with StarDist (Fiji)[56] and then tracking the labelled nuclei with TrackMate (Fiji)[57,58]. Further processing for the selection of trajectories and the quantification of instantaneous velocities was carried out with MATLAB. Only trajectories lasting for at least five consecutive frames have been considered for the evaluation of the root mean square velocity.

RAB5A-dependent collective motility

MCF10DCIS.com H2B-labelled cells (pSLIK-EV and pSLIK-RAB5A)[12,59] were subjected to two successive cycles of RNA interference (reverse and forward) with a specific siRNA against human IRSp53 (luciferase siRNA was used as a negative control) at the final concentration of 25 nM, according to manufacturer's instructions (RNAiMax, 13778150, Thermo Fisher). Cells were seeded in a six-well plate (1.5×10^6 cells per well) in complete medium. After 48 h from the first RNA interference cycle (reverse), 2.5 μg ml^{-1} of doxycycline was added to induce Rab5A expression and after an additional 6 h, time lapse was started. Collective motility was monitored by time-lapse imaging using an Olympus ScanR inverted microscope with a ×10 objective every 5 min for 24 h, at 37 °C in a humidified atmosphere with 5% CO_2. After the end of time-lapse imaging, cells were collected for RNA extraction and the analysis of RAB5A/IRSp53 expression by quantitative polymerase chain reaction.

The analysis of local and collective cell motility was performed via the PIV analysis of the time-lapse phase-contrast movies. The interrogation windows were 32 pixels (41.6 μm) on a side, with a 50% overlap between adjacent windows.

The instantaneous velocity of the centre of mass was computed as the average velocity $v_{CM}(t) = \langle v_i(t) \rangle_i$. The alignment between the local velocity $v_i(t)$ and the collective velocity $v_{CM}(t)$ was quantified within each grid point via the parameter $a_i = \frac{v_i \times v_{CM}}{||v_i|| ||v_{CM}||}$, where a value $a_i = 1$ ($a_i = -1$) indicates that the local velocity is parallel (antiparallel) to the mean direction of migration.

Spheroid formation and wetting

In the majority of wetting experiments, SCR and IRSp53_KD spheroids (from MCF10DCIS.com and HaCat cells) were obtained by seeding 5×10^3 cells in 200 μl of complete medium with 1 μg ml^{-1} of doxycycline in a 96-well Clear Round Bottom Ultra-Low Attachment Microplate (7007, Corning) and centrifuging them for 5 min at 300g, to allow the gathering of cells in the central area of each well. After 16 h, compact roundish spheroids are formed (one for each well). In specific experiments, spheroids of different sizes were obtained by seeding 2.5×10^2, 1×10^3 or 5×10^3 cells according to the protocol described above.

For wetting time-lapse experiments, 6–12 spheroids for each experimental condition were collected, pooled and seeded on a fibronectin-coated (final concentration, 10 μg ml^{-1}) six-well plate (one well for each condition). Spheroids were incubated for 1 h at 37 °C to

allow their attachment, and then, the spreading was monitored using an Olympus ScanR or iXplore inverted microscope with a ×4 objective every 10 min for 48 h (MCF10 DCIS.com) or every 20 min for 72 h (HaCat), at 37 °C in a humidified atmosphere with 5% CO_2. For wetting on different ECM substrates, spheroids were seeded on fibronectin (10 μg ml^{-1}), laminin (10 μg ml^{-1}) or collagen type I (10 μg ml^{-1}).

The contact area between the cell aggregates and the substrate was calculated at fixed time points (8 h, 16 h and 24 h) with Fiji. Its evolution over time was obtained via automatic segmentation of the time-lapse phase-contrast movies with custom MATLAB scripts. Only frames where the contact area had exceeded the initial spheroid projection of at least 20% were considered. The early stage spreading rate $\left(\frac{dA}{dt}\right)$ of each spheroid was then estimated by fitting the experimental curves with a linear fit of the kind $A(t) = \left(\frac{dA}{dt}\right)t + c$ over the first 24 h. The initial spheroid size was estimated from the spheroid projected area A_0 in the first frame of the time-lapse acquisition as the equivalent radius $R_0 = \sqrt{A_0/\pi}$.

Time-resolved cell velocity field was obtained via PIV analysis of time-lapse phase-contrast movies of spreading spheroids. PIV analysis was performed after masking the image portion outside the contact area to screen the background and calculate the velocity field only within the spreading monolayer. The same mask, obtained from contact area segmentation, was used for consecutive frames. The time interval between consecutive frames was 5 or 10 min and the interrogation windows were 8 or 16 pixels (26.1 or 20.8 μm) on a side.

The radial velocity component in each grid point was computed by considering the scalar product $v_{r,i} = v_i \times \hat{u}_r$, where $\hat{u}_r$ is the unit vector pointing from the centroid of the contact area to the centre of the ith interrogation window. We then computed the radial velocity profiles $v_r(r, t)$ at a given time t, by performing an azimuthal average over the grid points at the same distance r from the centroid.

The radial velocity profiles were first averaged over five consecutive frames and then fitted with the analytical solution of $v_r(r)$ obtained from the model, which has the following form:

$$\begin{aligned} v_r(r) = \Big(& R(R_1^2 - r^2)(2AL_c^2 + BR) I_1\left(\frac{R}{L_c}\right)^2 - BR^2(R_1^2 - r^2) I_0\left(\frac{R}{L_c}\right)^2 \\ & -2AL_c^2 r I_1\left(\frac{R}{L_c}\right) I_1\left(\frac{r}{L_c}\right) + L_c R(R_1^2 - r^2)(B - 2AR) I_0\left(\frac{R}{L_c}\right) I_1\left(\frac{R}{L_c}\right) \\ & +BL_c R_1 I_0\left(\frac{R_1}{L_c}\right) I_1\left(\frac{R_1}{L_c}\right)(R^2 + r^2) - BL_c r\,(R_1^2 + R_2^2) I_0\left(\frac{r}{L_c}\right) I_1\left(\frac{r}{L_c}\right) \\ & +2AL_c^2 R_1 I_1\left(\frac{R_1}{L_c}\right) I_1\left(\frac{R}{L_c}\right)(R^2 + r^2)\Big) / 2r I_1\left(\frac{R}{L_c}\right)^2 (R_1 + R^2), \end{aligned}$$

where $A = T_0 h/\eta$, $B = -\zeta/\eta$, L_c is the nematic length, R_1 is the position at which the radial velocity vanishes (representing the size of the solid core), R is the position of the spreading front and I_n is the modified Bessel function of the first kind and nth order.

The analytical solution was fitted only up to the radial position corresponding to 1.07% of r_p, where r_p is the position of the maximum of the experimental velocity profile, to reduce artefacts coming from boundary jags. For the fit to converge, R was fixed to the boundary value, whereas A, B, R_1 and L_c were kept as free fit parameters.

To perform single-cell tracking during spheroid spreading, SCR-H2B-GFP or IRSp53_KD-H2B-mCherry MCF10DCIS.com cells were used to generate spheroids as described above. Spheroid spreading was monitored using an IXplore system (Olympus), equipped with an Olympus IX83 SPIN microscope, a Hamamatsu ORCA-Fusion CMOS camera and a ×10 air objective (UPLFLN10X2PH Air, numerical aperture = 0.3, working distance = 10 mm). Live-cell conditions were achieved using an incubation chamber (CellVivo) maintained at 37 °C in an atmosphere of 5% CO_2. Olympus cellSens Dimension 4.2 software (Olympus) was used to manage the system.

Images were collected every 15 min for 25 h, by acquiring three different Z planes (step size, 5 μm) in the basal region of spheroids. Analysis of single-cell tracking was performed on the resulting maximum projections. Fluorescent nuclei have been first segmented with StarDist (Fiji)[56] and then tracked with TrackMate (Fiji)[57,58]. Further processing for the selection of trajectories and the quantification of their straightness was carried out with MATLAB. Only trajectories laying outside the initial spheroid projection and lasting for at least 15 consecutive frames have been considered for the evaluation of the straightness parameter, defined as the ratio between the end-to-end distance and the total trajectory length. The root mean square values of the tangential and radial velocity components have been quantified and compared when the radius of the spreading front has doubled the initial spheroid size by averaging over all cells in the spreading monolayer.

Traction force microscopy and analysis

SCR and IRSp53_KD spheroids were obtained by seeding 3×10^5 cells in 2 ml of complete medium with 1 μg ml^{-1} of doxycycline in AggreWellTM400 24-well microplate (34411, STEMCELL), according to manufacturer's instructions (one well for each condition). After 16 h, around 1,200 spheroids comprising ~250 cells each are obtained.

Traction force microscopy substrates were prepared as previously described[60]. In brief, a 15-kPa soft polydimethylsiloxane (PDMS) mixture was prepared by mixing DOWSIL CY 52-276 A and B components in 1:1 ratio (w/w). The mixture was spin coated onto glass coverslips (spin acceleration, 250 r.p.m. s^{-1}, 500 r.p.m. for 10 s and then 750 r.p.m. for 40 s) and polymerized overnight at 70 °C. PDMS layers were then activated with a 1:10 (v/v) solution of 3-aminopropyltriethoxysilane (Sigma-Aldrich) diluted in 100% laboratory-grade ethanol for 10 min at room temperature, washed thrice with 100% ethanol and dried at 70 °C for 10 min. Substrates were functionalized with a 2:1,000 (v/v) solution of fluorescent beads (FluoSpheres carboxylate-modified microspheres, 0.2 μm; Thermo Fisher Scientific) in MilliQ water, sonicated for 5 min, filtered through a 0.45-μm mesh and incubated with the activated soft PDMS surfaces for 10 min at room temperature. Substrates were then washed thrice with MilliQ water and dried at 70 °C for 10 min. TFM surfaces were kept at room temperature in the dark no longer than 2 weeks.

Soft PDMS substrates were coated with fibronectin (final concentration, 7 μg ml^{-1}) and spheroids were seeded on the gels after the harvesting step. Z stacks of fluorescent bead images and bright-field images were acquired every 10 min using a Nikon Ti2 microscope (as option equipped with CSU-W1 Yokogawa Spinning Disk unit) with a ×40 Nikon Plan-Apochromat air objective (numerical aperture = 0.95, working distance = 250 μm) and environment control (37 °C, 5% CO_2). At the end of the time-lapse imaging, spheroids were detached from the substrate using 10% (w/w) sodium dodecyl sulfate solution to acquire the relaxed position of the beads.

At each time point, the fluorescent beads within the gel were compared with a reference image obtained after cell detachment at the end of the experiment. Displacements were computed from bead trajectories obtained with single-particle tracking using TrackMate[57,58].

The instantaneous traction field was obtained from the displacement field using a custom MATLAB script implementing the Fourier transform traction cytometry scheme[61], with zeroth-order Tikhonov regularization[62].

Radial traction force components were computed and then azimuthally averaged over the points at the same distance r from the centroid of the contact area to get the radial traction profiles $T_r(r)$ at a given time t.

At each time t, we fit the experimentally measured radial traction force profiles with the equation $T_r(r) = -T_0 I_1\left(\frac{r}{L_c}\right)/I_1\left(\frac{R}{L_c}\right)$ predicted by the model[9], to estimate the maximum traction stress $T_0(t)$ and the nematic length $L_c(t)$.

The theoretical prediction was fitted only up to the radial position of the maximum of the experimental traction force profile, which sets the monolayer radius $R(t)$, discarding the outer region in which $T_r(r)$

drops because of poorly attached protrusions or long-range propagation of deformations in the elastic substrate[9].

We have also quantified the average radial traction in a core circular region and in an outer annular region by integrating the experimental radial traction profiles between $r = 0$ and $r = 0.75R$ and between $r = 0.75R$ and $r = R$, respectively, and dividing by the corresponding areas of the two internal and external regions.

Spheroid deformation in microfluidic device

SCR and IRSp53_KD spheroids were obtained by seeding 1.2×10^5 cells in 2 ml of complete medium with 1 μg ml^{-1} of doxycycline in AggreWellTM400 24-well microplate (34411, STEMCELL), according to the manufacturer's instructions (one well for each condition). After 16 h, around 1,200 spheroids comprising ~100 cells each are obtained.

Microfluidic devices were designed using AutoCAD (Autocad LT 2022, product version T.53.M.200) software, and silicon wafer masters were produced in a cleanroom environment (PoliFAB, Politecnico di Milano). The final devices were fabricated using moulds and elastomer PDMS (Dow Corning SYLGARD 184 Silicone Elastomer Kit 1.1 KG KIT). To fabricate the device, the cured replicas were peeled off the mould, punched and plasma bonded to thickness no. 1 glass coverslips (Prestige) that were precoated with a thin layer of PDMS. The bonded chips were kept at 80 °C for 20 min to secure a robust bonding. Afterwards, the silicon tubing was attached to the inlet and outlet of the devices. Before use, the devices were conditioned with 5% Pluronic F68 (P1300, Sigma-Aldrich) in PBS for 24 h to reduce the non-specific adsorption.

Microfluidic channels were incubated with an anti-adhesion coating solution (07010, STEMCELL) for 15 min, followed by a wash with media. Spheroids were introduced into the devices[35] at a constant flow rate of 3 ml h^{-1}: approximately 120 spheroids were introduced in 200 μl of media containing 25 mM of HEPES.

Deforming spheroids were tracked using a Thunder Leica microscope and a Photometrics Prime BSI Express sCMOS camera. Videos were created using a ×5 objective using the bright-field channel and obtaining 4–5-ms time-step sizes. Deformation passages were manually recorded by recording the inlet and outlet frames in which a spheroid passes through a constriction channel and multiplying by the time step.

Spheroid fusion

For fusion experiments, spheroids were obtained by seeding 500, 2,500 or 5,000 cells in a 96-well Clear Round Bottom Ultra-Low Attachment Microplate, as previously described. Once formed, two spheroids of the same size were collected and pooled in the same round-bottom well, in close proximity. EDTA was added at the final concentration of 0.3 mM, whereas seeding cells in the Ultra-Low Attachment Microplate to get spheroids. Dynamics of coalescence was monitored by acquiring images with an EVOS stereo-microscope using a ×4 objective after 1, 8, 24, 48 and 72 h. We followed the growth of the angle radius $r(t)$ of the neck between the coalescing spheroids. By fitting a simple exponential function of the kind $a(1 - e^{-\Gamma t})$ to the time evolution of the normalized variable $\Gamma \simeq /\eta R_0$, we estimated the initial fusion rate $\Gamma \simeq \sigma/\eta R_0$ and the amplitude term $a = (r/R)^2_\infty$, which is expected to tend to 1 for complete fusion.

Tipless AFM of apparent tension of spheroids

Stiffer tipless AFM cantilevers (CSC36/tipless/Cr–Au, NanoandMore) were calibrated on glass dishes in PBS at room temperature to calculate the spring constant and allowed to equilibrate to 37° for 30 min before the experimental measurements. These probes were utilized for their higher nominal spring constant value, allowing for higher applied forces to achieve greater deformations. After obtaining spheroids as described previously, they were adhered onto CellTak-coated FluoroDishes and transferred to the AFM stage in culture media. To generate larger, bulk deformations of spheroids (at least 10–15 μm), a larger force of 450 nN was applied. At least three consecutive deformations were collected on each spheroid with 20–30 s of relaxation between each curve. To account for the larger deformations in these curves and given the multicellular nature of these spheroids, the resultant tension value is defined as 'apparent' given the more heterogeneous nature of a spheroid. The first 10 μm of each force curve was used for quantifying the bulk tension values within each spheroid.

FLIM to measure membrane tension

Cells seeded as sparse islands or confluent monolayers were incubated in complete media supplemented with 1 μM of the Flipper-TR (Spirochrome/TebuBio SC020) for at least 2 h before the experiment.

FLIM experiments were performed on a Leica TCS SP8 laser-scanning confocal module mounted on a Leica DMi 8 inverted microscope, equipped with a time-correlated single-photon-counting module (PicoQuant), on-stage environmental chamber (Okolab) and controlled by the software Leica Application Suite X (v. 3.5.2.18963).

For image acquisition, an HC PL APO CS2 ×40/1.30 oil-immersion objective was used. Samples were excited with a pulsed white light laser operating at 20-MHz frequency, 1–5% power and the excitation wavelength set at 488 nm. The emission signal was collected through a 550–650-nm bandpass filter using hybrid detectors in the photon-counting mode, pinhole set to 2 Airy unit and 200-Hz scanning speed to maximize photon detection. A signal intensity of at least 10^4 Airy unit and an average of 300 photons per pixel was collected for each image.

Lifetime analysis was performed on the software SymPhoTime64 (PicoQuant, version 2.4.4874). Specifically, the spatial resolution was sacrificed in favour of the maximum fitting likelihood and 512 × 512 raw images were binned 2× (256 × 256). The two-exponential tail-fit method was applied to extract the fluorescence lifetimes and excludes the potential contribution of the sample excitation during laser pulses. Given the negligible contribution of τ_1 compared with τ_2 of the decay curve, the average lifetime was calculated for whole images, setting the pixel with >20–30 event counts to NaN. For island analysis, event count images were used to create an arbitrary binary mask of cell–cell junctions, to avoid contribution from non-junctional portions of the cells to lifetime calculations. Mean lifetime values for each thresholded image were obtained using Fiji.

Blebbing analysis

SCR and IRSp53_KD cells were detached by trypsinization and resuspended by gentle pipetting for 5 min. Bleb formation and reabsorption over time was monitored by a DeltaVision microscope with a ×40 oil objective every 10 s for 5 min. The blebbing dynamics was quantified by segmentation of cells with a custom Fiji plug-in[63]. After choosing the object to measure for each cell, the plug-in applies a WEKA custom model[64] to identify the objects and extrapolates the area variation for each frame.

Nanomechanical AFM mapping of MCF10DCIS.com monolayer

SCR, IRSp53_KD and AFD_KD cells were seeded in confluent conditions on 35-mm glass-bottom dishes (FluoroDish FD35–100, World Precision Instruments), in complete medium with 1 μg ml^{-1} of doxycycline. The day after, monolayers were rinsed with PBS 1× several times and taken to the NanoWizard 4XP AFM system (Bruker). After calibrating a PFQNM-LC-V2 live-cell probe (Bruker) and letting it equilibrate to 37 °C, the cells were placed on the AFM stage to image. Cells were scanned in the quantitative imaging mode to generate high-spatial-resolution maps to quantify Young's modulus using a modified Hertz contact model for paraboloidal tips[65]. Scans were taken at 256 × 256 resolution with a 1-nN force setpoint, 1,500-nm Z range and 100 μm s^{-1} of ramp speed over an area of 50 × 50 μm^2.

Laser ablation on junctions and apical cortex

SCR and IRSp53_KD cells (stably expressing EGFP–CAAX as membrane reporter) or AFD_KD cells (stably expressing mCherry–CAAX) were

seeded in confluent conditions (at the jamming density) onto Nunc Glass Base dish (diameter, 27 mm) in complete medium with 1 μg ml^{-1} of doxycycline.

After 48–72 h, monolayers were subjected to targeted laser ablation. Experiments were performed using a Leica Stellaris DIVE combined with a femtosecond pulsed Spectra Physics Laser capable of priming two-photon excitation. The ablation was performed using a 750-nm wavelength. Imaging was performed with single-photon excitation in a regular confocal fashion. The objective used was an HC PL APO ×63/1,2 W UVIS CS2. For laser ablation on junctions, the distance between vertices (vertex separation) defining the ablated contact was measured as a fraction of time. Distance values were subtracted from the initial contact length. The values were then calculated as a function of time, and the initial recoil values for each contact were obtained by a nonlinear regression of the data to the following equation: $f(t) = (\text{initial recoil}/k)(1 - e^{-kt})$ (refs. 7,66). For laser ablation of the apical cortex, changes in the cellular area (measured by the CAAX signal as a proxy for the cell perimeter) were quantified as a fraction of time using Fiji software[29].

CLEM

Electron microscopy examination and CLEM were performed as previously described[21,67,68]. In brief, MCF10DCIS.com SCR and IRSp53_KD cells (stably expressing EGFP–E-cadherin as a junctional reporter) were trypsinized to a single-cell suspension at 4 × 10^4 cells ml^{-1} in complete medium containing 2% Matrigel (BD Biosciences). Cell–medium–Matrigel suspensions (350 μl) were plated in 35-mm dishes with gridded coverslips (P35G-1.5–14-CGRD, MatTek), precoated with 20 μl of Matrigel (10 mg ml^{-1}). Then, 2% Matrigel complete medium was added to 2 ml of complete medium with 1 μg ml^{-1} of doxycycline. After 72–96 h, the obtained spheroids were stained with NucBlue Live ReadyProbes and identified on grids by confocal microscopy. The fluorescence images for the CLEM data were acquired on a Leica SP8 DLS confocal microscope, using an HC PL FLUOTAR ×20/0.5 objective.

Electron microscopy. A brief description of each process is presented below.

Embedding. Spheroids grown on MatTek glass-bottom dishes were fixed with a 2.5% paraformaldehyde and 2.5% glutaraldehyde (EMS) mixture in 0.2 M of sodium cacodylate (pH 7.2) for 2 h at room temperature, followed by three washes in 0.2 M of sodium cacodylate (pH 7.2) at room temperature. Then, the spheroids were incubated in a 1:1 mixture of 2% osmium tetraoxide and 3% potassium ferrocyanide for 1 h at room temperature followed by rinsing for three times in cacodylate buffer. Afterwards, the samples were sequentially treated with 0.3% thiocarbohydrazide in 0.2 M of cacodylate buffer for 15 min and 1% osmium tetraoxide in 0.2 M of cacodylate buffer (pH 6.9) for 30 min. The samples were then rinsed with 0.1 M of sodium cacodylate (pH 6.9) buffer until all traces of the yellow osmium fixative were removed and then it was washed in deionized water, treated with 1% uranyl acetate in water for 1 h and washed in water again. Finally, the samples were subjected to dehydration in ethanol and embedded in epoxy resin at room temperature and polymerized for at least 72 h in a 60 °C oven[67].

Sectioning. As described above, the spheroid of interest was selected during the optical sectioning and *Z* stacking using confocal microscopy. During *Z* stacking, the distance between the bottom and surface of the spheroid was estimated. The embedded samples were then sectioned with a diamond knife (DiATOME) using a Leica EM UC7 ultramicrotome. For the trimming and advance to the region of interest, we used the DiATOME diamond trimming blades (trim tool 45 and histo; DiATOME). To avoid mistakes, we took into consideration the possible 'shrinkage' of the matrix during its dehydration and embedding into Epon. Thus, when only 3 μm was left before the beginning of the cell surface, we replaced the trimming histo-knife with an Ultra 35 knife (DiATOME), and then cut two 200-nm sections and then a small series of 70-nm sections. Sections were analysed with a Tecnai 20 High Voltage EM (Thermo Fisher Scientific) operating at 200 kV.

Immunofluorescence on MCF10DCIS.com monolayers

SCR and IRSp53_KD cells were seeded in confluent conditions (at the jamming density) in μ-Slide 8 well ibiTreat chambers (ibidi, 80826) in complete medium with 1 μg ml^{-1} of doxycycline. After 16 h, monolayers were fixed with 4% paraformaldehyde for 20 min at room temperature. Cells were then permeabilized and blocked with PBS 0.1% Triton X-100 and 0.2% bovine serum albumin for 20 min at room temperature. Incubation with primary antibody solution (1% bovine serum albumin in PBS 1×; Supplementary Table 3) was performed overnight at 4 °C in a wet chamber protected from dark. After three washes of 5 min each with PBS 1×, incubation with secondary antibody solution (PBS 1×; Supplementary Table 3) was performed for 1.5 h at room temperature. After three washes of 5 min each with PBS, nuclei were stained with DAPI (1:1,000 in PBS 1×) and samples were stored in PBS at 4 °C till acquisition.

Samples were imaged using a Leica SP8 DLS microscope (lasers used were 405, 488, 561 and 647 nm) with a ×63 (1.4 correction) oil objective. Confocal sections on the *z* axis were acquired with 0.5-μm step size and resliced on the *y* axis using ImageJ, to get maximum projections of actin staining (TRITC–phalloidin). A Leica algorithm allowing for computational clearing (Thunder) was also used to image phallodin-positive intercellular spaces in the MCF10DCIS.com monolayer.

Clinical cohorts and histopathological evaluation

A TMA comprising a retrospective consecutive cohort of 1,755 female patients, from the European Institute of Oncology in Milan[53,54], with complete clinicopathological follow-up, was used. All patients provided written informed consent and underwent surgical procedures. Sections obtained from paraffin-embedded tissues were stained with mouse monoclonal anti-IRSp53, as already described[21], and analysed with a Scan Scope XT device and the Aperio Digital pathology system software (Aperio, Leica). Patients were stratified according to the immunohistochemical pattern distribution of IRSp53 (apical–membrane distribution versus cytosolic distribution) in the primary tumour. The association between IRSp53 apical–membrane distribution or cytosolic distribution and different clinicopathological parameters was evaluated using Fisher's exact test.

Statistical analysis and data reproducibility

All quantitative data are presented as scatter plots with bars indicating the mean ± s.d. of independent biological replicates, unless stated otherwise. The number of independent experiments and the number of samples analysed for each experiment are reported in the corresponding figure legends. Exact *P* values, when statistically relevant, are indicated in the figures and summarized in Supplementary Table 4. No statistical methods were used to predetermine the sample size. No data were excluded from the analyses. Experiments were not randomized, and investigators were not blinded to allocation during experiments or outcome assessment.

For all the quantitative analyses, the unit of analysis was defined as the smallest independently measurable biological entity subjected to the experimental intervention. Depending on the assay, this corresponded to individual spheroids, individual cells, individual cell collectives or independent fields of view within confluent monolayers. These units were independently generated and analysed both within and across experiments. As variability between units within a single experiment was comparable with variability observed between independent experiments, data from multiple experiments were pooled

for statistical analysis. Pooling was performed only after confirming the reproducibility of the measured distributions across biological replicates, with no detectable differences in effect size or variance between experiments. Accordingly, for each figure, both the number of samples analysed and the number of independent experiments performed are reported.

Reporting summary

Further information on research design is available in the Nature Portfolio Reporting Summary linked to this article.

Data availability

Data supporting the findings of this study are available within the Article and its Supplementary Information. Source data are provided with this paper.

References

56. Schmidt, U., Weigert, M., Broaddus, C. & Myers, G. Cell detection with star-convex polygons. In *Medical Image Computing and Computer Assisted Intervention* (eds Frangi, A. F. et al.) 265–273 (Springer, 2018).
57. Ershov, D. et al. TrackMate 7: integrating state-of-the-art segmentation algorithms into tracking pipelines. *Nat. Methods* **19**, 829–832 (2022).
58. Tinevez, J. Y. et al. TrackMate: an open and extensible platform for single-particle tracking. *Methods* **115**, 80–90 (2017).
59. Frittoli, E. et al. Tissue fluidification promotes a cGAS-STING cytosolic DNA response in invasive breast cancer. *Nat. Mater.* **22**, 644–655 (2023).
60. Teo, J. L., Lim, C. T., Yap, A. S. & Saw, T. B. A biologist's guide to traction force microscopy using polydimethylsiloxane substrate for two-dimensional cell cultures. *STAR Protoc.* **1**, 100098 (2020).
61. Butler, J. P., Tolic-Norrelykke, I. M., Fabry, B. & Fredberg, J. J. Traction fields, moments, and strain energy that cells exert on their surroundings. *Am. J. Physiol. Cell Physiol.* **282**, C595–C605 (2002).
62. Sabass, B., Gardel, M. L., Waterman, C. M. & Schwarz, U. S. High resolution traction force microscopy based on experimental and computational advances. *Biophys. J.* **94**, 207–220 (2008).
63. Schindelin, J. et al. Fiji: an open-source platform for biological-image analysis. *Nat. Methods* **9**, 676–682 (2012).
64. Frank, E. & Hall, M. A. *Data Mining: Practical Machine Learning Tools and Techniques* (Morgan Kaufmann, 2011).
65. Guo, Z. et al. A modified Hertz model for finite spherical indentation inspired by numerical simulations. *Eur. J. Mech. A. Solids* **83**, 104042 (2020).
66. Liang, X., Michael, M. & Gomez, G. A. Measurement of mechanical tension at cell-cell junctions using two-photon laser ablation. *Bio Protoc* **6**, e2068 (2016).
67. Beznoussenko, G. V. & Mironov, A. A. Correlative video-light-electron microscopy of mobile organelles. *Methods Mol. Biol.* **1270**, 321–346 (2015).
68. Mironov, A. A. & Beznoussenko, G. V. Algorithm for modern electron microscopic examination of the golgi complex. *Methods Mol. Biol.* **2557**, 161–209 (2023).

Acknowledgements

We thank S. Barozzi and F. Casagrande of the Advanced Light Microscopy Facility at IFOM for technical assistance in advanced imaging acquisition; the Cellular and Preclinical Models Facility at IFOM for technical assistance; the Flow Cytometry Facility at IFOM for technical assistance; V. Dall'Olio and L. Tizzoni at Cogentech for quantitative reverse-transcription polymerase chain reaction services; M. Goudreault and M. J. Smith (Institut de recherche en immunologie et en cancérologie (IRIC), Université de Montréal) for the GST–AFD constructs. The work is supported by ERC-Synergy (grant number 801 101071470), AIRC IG (grant number 22821), AIRC 5x1000 (number 22759), the Italian Ministry of University and Research (PRIN202223GSCIT_01/G53D23002570006/20229RM8A_001;COMBINE/G53D23007040001/P2022RH4HH002;PNRR_CN3RNA_SPOKE/G43C22001320007) to G.S.; AIRC MFAG-22083 to F.G.; Intramural funding of the Division of Intramural Research Program at the National Institutes of Biomedical Imaging and Bioengineering with grant number ZIA-EB000094 and the National Institutes of Health central funds for the NIH Distinguished Scholars Program award to A.X.C.-R. and A.E.M.; funding through the Max Planck School Matter to Life supported by the German Federal Ministry of Education and Research (BMBF) and through High-Tech Agenda Bavaria to E.A.C.-A.; AIRC IG number 24976, the Italian Ministry of University and Scientific Research, PRIN PNRR P2022F3YRF to P.M.; AIRC IG 2022-ID 27101 to N.C.G.; AIRC IG number 18629 to M.M.; Associazione Italiana per la Ricerca sul Cancro (AIRC) (IG-23049 and IG-31110), the Italian Ministry of University and Scientific Research (MIUR/PRIN2020) and the Italian Ministry of Health with Ricerca Corrente and 5x1000 funds to S.P.; ERC-CoG2020 number 101002280, AIRC IG number 24415 and the Italian Ministry of University and Scientific Research, PRIN 2022, prot.2022W93FTW to S.S.; Fondazione Veronesi Post-doctoral fellowship 2025 to S. Marchesi; AIRC MFAG 2022 (grant number 27616) to B.J.G.; and Fondazione Cariplo Young Investigator Grant (number 2021-1507) to A.G.

Author contributions

S. Marchesi and A.D. designed and performed the majority of the experiments and edited the manuscript. C.G. and F.G. conceived the mathematical model, performed all the biophysical analysis (unjamming to jamming, collective motility, spheroid wetting and spheroid fusion) and contributed to editing the manuscript. A.E.M. and A.X.C.-R. performed and analysed all the AFM microscopy studies. G.L. performed the traction force experiments. C.L. performed the traction force biophysical analysis. Z.L., D.P. and A.D. designed, performed and analysed the advanced light microscopy studies (confocal two-photon laser ablation and image 3D reconstruction). G.V.B., E.A., Z.L., A.D. and A.A.M. performed the CLEM studies. B.J.G. designed and realized the microfluidic device for spheroid deformation and performed all the experiments and analysis with S. Marchesi. E.A. derived the mammary epithelial cells from mice mammary gland and performed the wetting assay with S. Marchesi. E.M. and S. Magni analysed wound healing, junctional laser ablation, cell blebbing and focal adhesion experiments. A.G. and A.D. performed and analysed the FLIM microscopy studies. A.F.B. performed and analysed all the fluorescence-activated cell sorting experiments. A.S. performed the FIB–SEM experiments. D.A.v.F. performed and analysed spheroid wetting on different ECM substrates. M.M. performed the computational prediction structural model of the IRSp53:AFD interaction, using the AlphaFold3 server. P.M. analysed the one-dimensional motility experiments. S.P., S.F. and G.B. analysed the IRSp53 expression and localization on TMA from the European Institute of Oncology in Milan. S.P., S.S., N.C.G., E.A.C.-A. and A.X.C.-R. supervised the experimental procedures. A.X.C.-R., F.G., G.S. and A.D. conceived the whole study, wrote the manuscript and supervised the whole project.

Competing interests

The authors declare no competing interests.

Additional information

Extended data is available for this paper at https://doi.org/10.1038/s41563-026-02553-2.

Supplementary information The online version contains supplementary material available at https://doi.org/10.1038/s41563-026-02553-2.

Correspondence and requests for materials should be addressed to Giorgio Scita.

Peer review information *Nature Materials* thanks Josef Käs, Shiro Suetsugu and the other, anonymous, reviewer(s) for their contribution to the peer review of this work.

https://doi.org/10.1038/s41563-026-02553-2

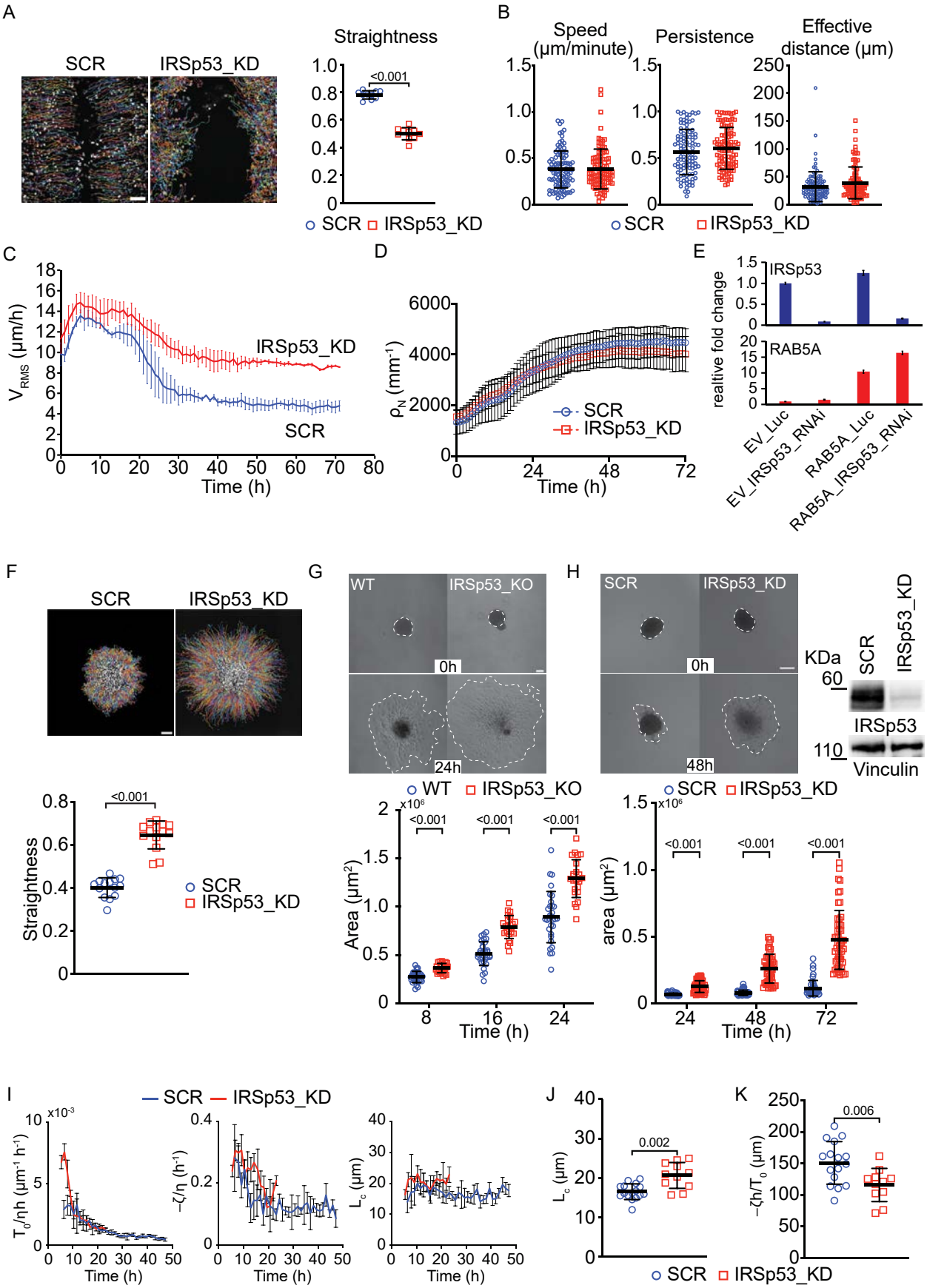

Extended Data Fig. 1 | See next page for caption.

https://doi.org/10.1038/s41563-026-02553-2

Extended Data Fig. 1 | Quantitative analysis of collective migration and spheroids active wetting. a. Scratch-wound migration of SCR-H2B-GFP and IRSp53_KD–H2B-mCherry MCF10DCIS.com monolayers (Supplementary Movie S2). Left: representative still images with single-cell trajectories (SCR: 6 h 40 min; IRSp53_KD: 24 h). Scale bar, 100 µm. Right: trajectory straightness (see Methods). Mean of 10 fields of view ± SD (n = 2 independent experiments). **b**. Time-lapse imaging of SCR or IRSp53_KD MCF10DCIS.com cells on fibronectin-coated linear patterns (10 µm width; 10 µg/ml) (see Methods) (Supplementary Movie S3). Left: still images; scale bar, 50 µm. Right: mean instantaneous speed and mean persistence (see Supplementary Methods). Mean ± SD (n = 100 cells/condition; 3 independent experiments). **c**. Root mean square velocity (V_{RMS}) over time from single-cell tracking of SCR-H2B-GFP and IRSp53_KD–H2B-mCherry MCF10DCIS.com cells seeded at jamming density (Supplementary Movie S5). Mean ± SD (n = 16 fields; 2 independent experiments). **d**. Nuclear density over time for jammed SCR-H2B-GFP and IRSp53_KD–H2B-mCherry MCF10DCIS.com monolayers (Fig. 1c; Supplementary Movie S5). Mean ± SD (n = 16 fields; 2 independent experiments). **e**. qRT–PCR validation of IRSp53 and RAB5A mRNA levels (related to Fig. 1d). Mean ± SD (n = 3 technical replicates). **f**. Spreading of SCR-H2B-GFP and IRSp53_KD-H2B-mCherry MCF10DCIS.com spheroids on fibronectin (Supplementary Movie S8). Top: maximum projections at 25 h with trajectories; scale bar, 200 µm. Bottom: trajectory straightness (see Methods). Mean ± SD (n = 14 fields; 2 independent experiments). **g**. WT vs IRSp53_KO mouse mammary epithelial spheroids: spreading on fibronectin (Supplementary Movie S9). Still images at indicated times; scale bar, 100 µm. Quantified spreading area (ImageJ). Mean ± SD (n = 31 WT, 25 IRSp53_KO spheroids; 3 independent experiments). **h**. HaCaT SCR vs IRSp53_KD spheroids spreading on fibronectin (Supplementary Movie S10). Still images at indicated times; scale bar, 200 µm. Spreading area (ImageJ): mean ± SD (n = 46 SCR, 51 IRSp53_KD spheroids; 3 independent experiments). Right: WB with indicated antibodies. **i**–**m**. Spreading parameters from segmentation and PIV of SCR vs IRSp53_KD spheroids (related to Fig. 2b–f). **i**, Time evolution of A, B and Lc. Mean ± SD (n = 7 SCR, 5 IRSp53_KD spheroids). **j**, Nematic length Lc at matched spreading. Mean ± SD (n = 16 SCR, 11 IRSp53_KD spheroids; 3 independent experiments). **k**, Ratio B/A = $-\zeta h/T_0$. Mean ± SD (n = 16 SCR, 11 IRSp53_KD spheroids; 3 independent experiments). Statistical tests are in Supplementary Table 4, P values are in the graphs.

https://doi.org/10.1038/s41563-026-02553-2

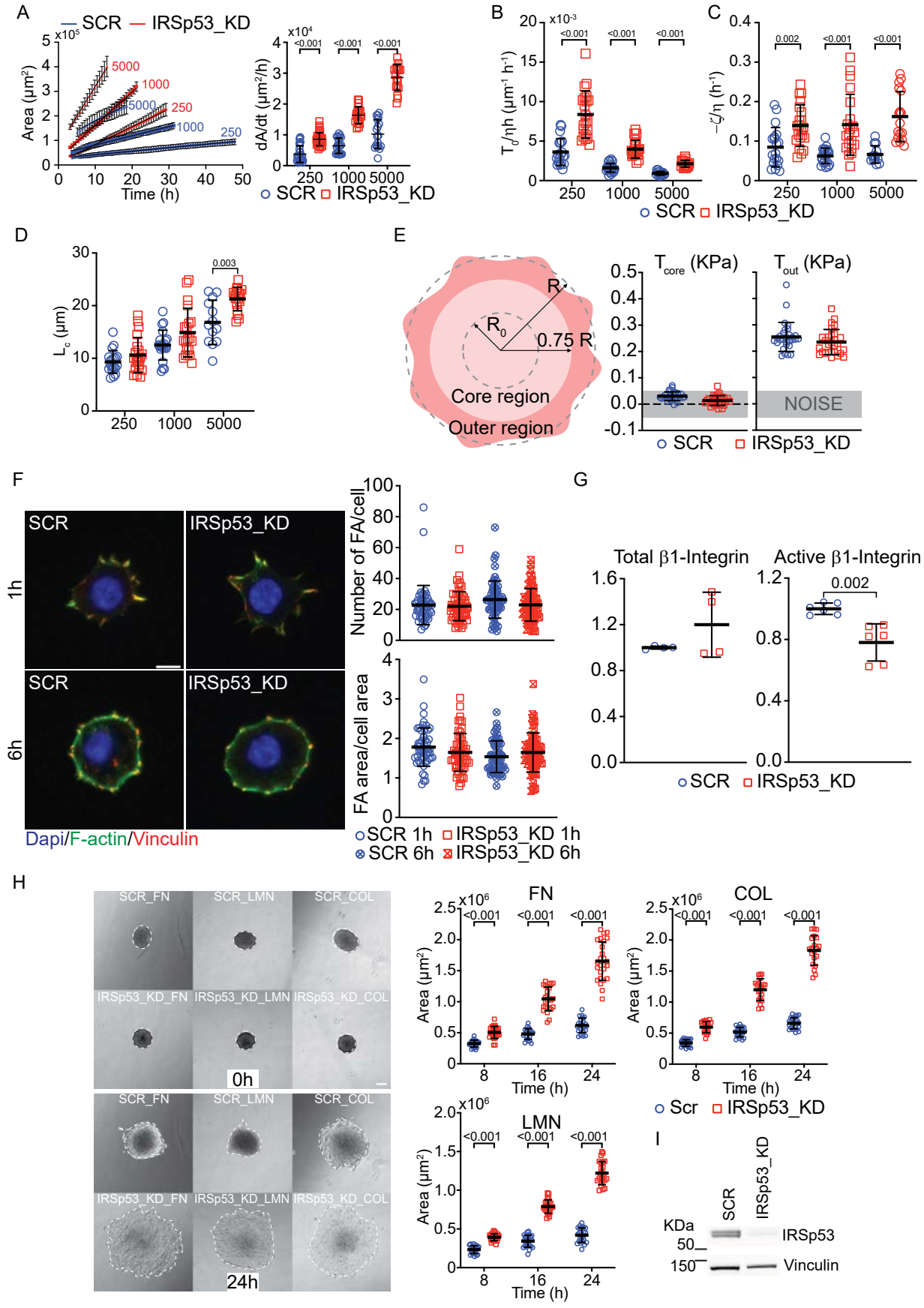

Extended Data Fig. 2 | See next page for caption.

https://doi.org/10.1038/s41563-026-02553-2

Extended Data Fig. 2 | Quantitative analysis of spheroids active wetting dynamics and cell-substrate adhesion. a. Left: spreading area over time for spheroids of different initial sizes, quantified by semi-automatic MATLAB segmentation; black lines, linear fits per condition. Right: single spheroid spreading rates (dA/dt). Mean ± SD (n = 29 SCR-250, 34 IRSp53_KD-250, 21 SCR-1000, 20 IRSp53_KD-1000, 18 SCR-5000, 18 IRSp53_KD-5000 spheroids; 3 independent experiments). **b-e**. Spreading parameters from image segmentation and PIV for different spheroid sizes. **B**. A. **C**. B. **D**. Nematic length *Lc*. Mean ± SD (spheroids: n = 19 SCR-250, 21 IRSp53_KD-250; n = 21 SCR-1000, 20 IRSp53_KD-1000; n = 13 SCR-5000, 17 IRSp53_KD-5000; 3 independent experiments). **e**. Average radial traction computed by partitioning spreading spheroids (radius R) into an inner disk (radius 0.75 R) and an outer annulus (0.75R–R) near the leading edge. Mean ± SD (n = 29 SCR, 28 IRSp53_KD spheroids; 3 independent experiments). **f**. IRSp53 loss does not alter focal adhesions. Doxycycline-treated SCR and IRSp53_KD MCF10DCIS.com cells were plated on fibronectin-coated (10 µg/ml) glass-bottom dishes, fixed at 1 h or 6 h, stained for Vinculin (red), F-actin (FITC-phalloidin, green), and DAPI (blue), and imaged by TIRF. Left: representative images (1 h, 6 h). Scale bar, 10 µm. Right: focal adhesions/cell and focal adhesion area/cell area (ImageJ; see Methods). Mean ± SD (1 h: n = 53 cells/1210 adhesions SCR, 56/1235 IRSp53_KD; 6 h: n = 58/1546 SCR, 66/1515 IRSp53_KD; 2 independent experiments). **g**. IRSp53 silencing does not increase β1-integrin surface levels. FACS for total (left) and active (right) β1-integrin; data as mean fluorescence intensity normalized to SCR. Mean ± SD (total: n = 4 technical replicates; 2 independent experiments; active: n = 6 technical replicates; 3 independent experiments). **h**. SCR and IRSp53_KD spheroids (ultra-low adhesion) replated on fibronectin, laminin, or collagen I (all 10 µg/ml) and imaged by time-lapse (Supplementary Movie S12). Left: stills at indicated times; scale bar, 200 µm. Right: spreading area (ImageJ). Mean ± SD (n = 23 SCR_FN, 28 IRSp53_KD_FN; n = 24 SCR_LMN, 19 IRSp53_KD_LMN; n = 25 SCR_COL, 20 IRSp53_KD_COL spheroids; 2 independent experiments). **i**. Immunoblots of SCR and IRSp53_KD MCF10DCIS.com with indicated antibodies. Statistical tests are in Supplementary Table 4, P values are in the graphs.

https://doi.org/10.1038/s41563-026-02553-2

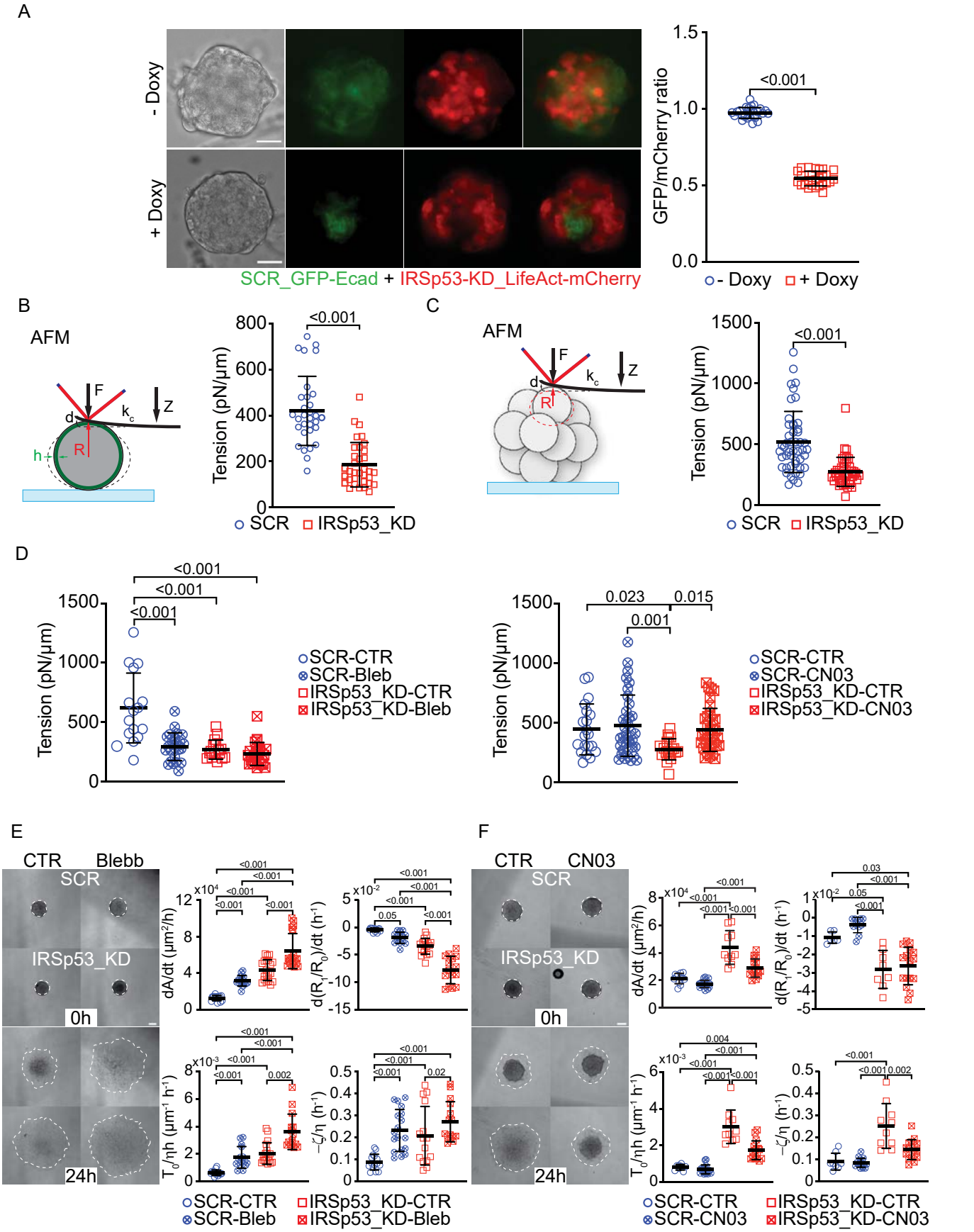

Extended Data Fig. 3 | See next page for caption.

https://doi.org/10.1038/s41563-026-02553-2

Extended Data Fig. 3 | IRSp53 couples single-cell mechanics to tension to control the wetting transition. a. Spheroid sorting. SCR-GFP-E-cadherin and IRSp53_KD-mCherry-LifeAct MCF10DCIS.com cells, untreated (-Doxy) or doxycycline-treated (+Doxy), were mixed 1:1, cultured for 48 h in ultra-low adhesion to form spheroids, and imaged (EVOS). Left: representative brightfield and fluorescence images; bar, 200 µm. Right: sorting quantified as GFP/mCherry fluorescent area ratio in mixed spheroids generated from SCR-GFP−H2B and IRSp53_KD−mCherry−H2B cells (not shown) by contouring fluorescent areas in ImageJ. Mean ± SD (n = 27 −Doxy, 26 +Doxy mixed spheroids; 3 independent experiments). **b**. AFM probing of weakly adherent single cells. Left: schematic of a nonadherent cell deformed with a tipless cantilever; applied force (F), cantilever deflection (d), piezo displacement (Z), cantilever spring constant (kc), initial cell radius (R) and cortical actin thickness (h) are indicated[1]. Right: cortical actomyosin tension in doxycycline-treated SCR vs IRSp53_KD cells, extracted at Z ≤ 1000 nm. Mean ± SD (n = 36 cells; 3 independent experiments). **c**. AFM probing of spheroids. Left: schematic of weakly adherent spheroids (apical cell) deformed with a tipless cantilever (F, d, Z, kc, R)[1]. Right: cortical actomyosin tension in 500-cell spheroids (Z ≤ 1000 nm). Mean ± SD (n = 48 SCR, 42 IRSp53_KD cells; 3 independent experiments). **d**. Pharmacological modulation in 500-cell spheroids (Z ≤ 1000 nm). Left: DMSO vs 5 µM Blebbistatin. Mean ± SD (n = 16 SCR, 24 SCR+Blebb, 16 IRSp53_KD, 24 IRSp53_KD+Blebb cells; 3 independent experiments). Right: vehicle vs 10 µg/ml CN03. Mean ± SD (n = 20 SCR, 35 SCR + CN03, 20 IRSp53_KD, 35 IRSp53_KD + CN03 cells; 3 independent experiments). **e**. Blebbistatin and spreading. Spheroids were treated 6 h before plating with DMSO (CTR) or 5 µM Blebbistatin, replated on fibronectin-coated 6-well plates and imaged by time-lapse (Supplementary Movie S14). Left: representative stills; scale bar, 200 µm. Right: segmentation/PIV-derived parameters: dA/dt, normalized core-melting rate d(R1/R0)/dt, traction/viscosity ratio, and A and B. Mean ± SD (3 independent experiments; dA/dt: n = 15 SCR, 15 SCR-Bleb, 21 IRSp53_KD, 18 IRSp53_KD-Bleb; d(R1/R0)/dt, A, B: n = 11 SCR, 13 SCR-Bleb, 20 IRSp53_KD, 18 IRSp53_KD-Bleb spheroids). **f**. CN03 and spreading. As in E, with vehicle or 10 µg/ml CN03 (Supplementary Movie S15). Left: stills; scale bar, 200 µm. Right: dA/dt, d(R1/R0)/dt, traction/viscosity ratio, and contractility/traction ratio. Mean ± SD (3 independent experiments; dA/dt: n = 11 SCR, 19 SCR-CN03, 10 IRSp53_KD, 16 IRSp53_KD-CN03; d(R1/R0)/dt: n = 6 SCR, 11 SCR-CN03, 8 IRSp53_KD, 16 IRSp53_KD-CN03; A, B: n = 8 SCR, 16 SCR-CN03, 10 IRSp53_KD, 16 IRSp53_KD-CN03 spheroids). Statistical tests are in Supplementary Table 4, P values are in the graphs.

https://doi.org/10.1038/s41563-026-02553-2

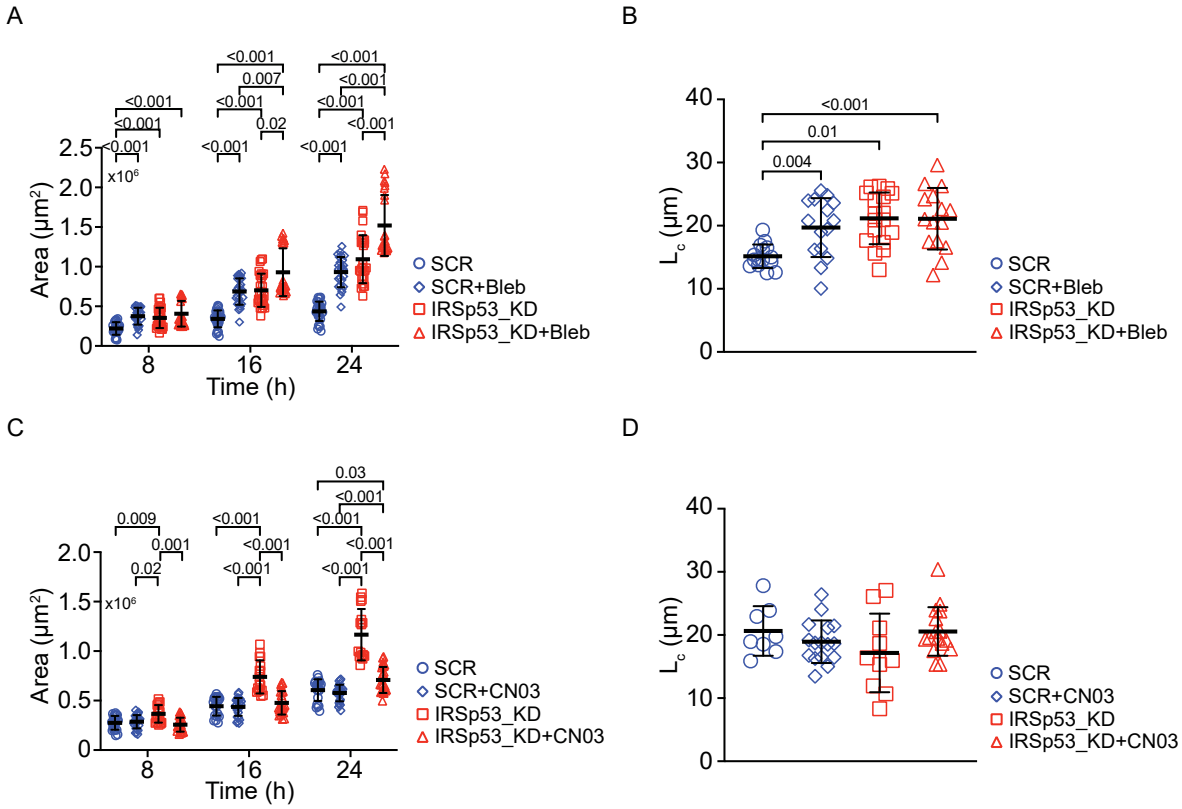

Extended Data Fig. 4 | Quantitative analysis of spheroid active wetting upon pharmacological actomyosin perturbation. a. The spreading area of wetting spheroids (Extended Data Fig. 3e and Supplementary Movie S14) at the indicated time points was manually quantified using ImageJ. Mean ± SD (n = 29 SCR CTR, 26 SCR+Blebb, 27 IRSp53_KD CTR, 24 IRSp53_KD+Blebb spheroids; 3 independent experiments). **b**. Nematic length L_c obtained from image segmentation and PIV analysis of MCF10DCIS.com spheroids upon Blebbistatin treatment (Extended Data Fig. 3e and Supplementary Movie S14). Mean ± SD (n = 15 SCR, n = 15 SCR+Blebb, n = 18 IRSp53_KD, n = 15 IRSp53_KD+Blebb cells; 3 independent experiments) **c**. The spreading area of wetting spheroids (Extended Data Fig. 3f and Supplementary Movie S15) at the indicated time points was manually quantified using ImageJ. Mean ± SD (n = 21 SCR CTR, 26 SCR + CN03, 17 IRSp53_KD CTR, 24 IRSp53_KD + CN03 spheroids; 3 independent experiments). **d**. Nematic length L_c obtained from image segmentation and PIV analysis of MCF10DCIS.com spheroids upon CN03 treatment (Extended Data Fig. 3f and Supplementary Movie S15). Mean ± SD (n = 8 SCR, n = 16 SCR + CN03, n = 10 IRSp53_KD, n = 16 IRSp53_KD + CN03 cells; 3 independent experiments). Statistical tests are in Supplementary Table 4, P values are in the graphs.

https://doi.org/10.1038/s41563-026-02553-2

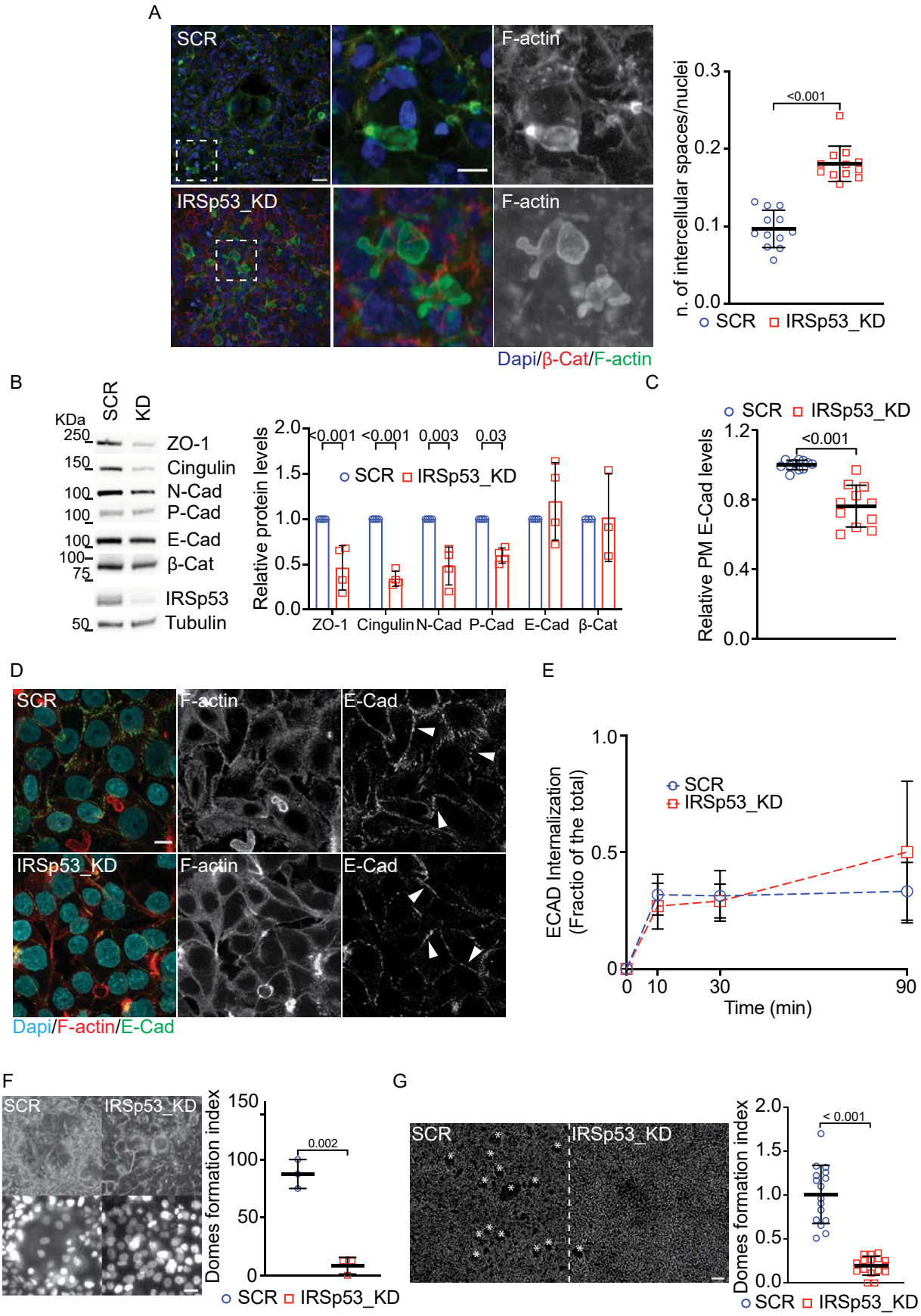

Extended Data Fig. 5 | See next page for caption.

https://doi.org/10.1038/s41563-026-02553-2

Extended Data Fig. 5 | IRSp53 loss disrupts epithelial cohesion and junctional homeostasis. a. Increased intercellular spaces upon IRSp53 silencing. SCR and IRSp53_KD MCF10DCIS.com cells were seeded at jamming density and fixed 96 h post-seeding, stained for α-catenin (red), F-actin (FITC–phalloidin, green) and nuclei (DAPI, blue). Representative deconvolved 3D stacks acquired with Leica THUNDER are shown (Supplementary Movies S20–21). Bar, 10 µm. Right: intercellular spaces quantified as number of spaces per nuclei (mean ± SD; n = 12 fields; 2 independent experiments; ~230 nuclei/field SCR, ~247 nuclei/field IRSp53_KD). **b**. Junctional protein levels are altered by IRSp53 removal. Doxycycline-treated SCR or IRSp53_KD cells seeded at jamming density were analysed by immunoblotting 4 days after seeding. Left: WB for indicated junctional proteins and IRSp53. Right: densitometric quantification normalized to tubulin (ImageJ). Mean ± SD (n = 4 independent experiments for ZO-1, cingulin, E-cadherin, P-cadherin, N-cadherin; n = 3 independent experiments for β-catenin). **c**. Reduced E-cadherin at the plasma membrane. Flow cytometry of surface E-cadherin in SCR vs IRSp53_KD MCF10DCIS.com cells, shown as mean fluorescence intensity (MFI) normalized to SCR. Mean ± SD (n = 11 technical replicates; 5 independent experiments). **d**. Junctional localization of E-cadherin. Confocal sections (5 µm above the bottom adherent surface) of jammed monolayers fixed 96 h post-seeding and stained for E-cadherin (green), F-actin (TRITC–phalloidin, red) and DAPI (blue). Arrowheads indicate E-cadherin at cell–cell junctions. Bar, 10 µm. **e**. E-cadherin endocytosis. FACS-based assay of ECAD internalization in SCR vs IRSp53_KD cells; MFI (fraction of SCR ± SD) at 10, 30 and 90 min. Mean ± SD (n = 3 independent experiments). **f**. Dome formation dynamics. SCR-H2B-GFP and IRSp53_KD–H2B-mCherry cells seeded at jamming density were imaged by time-lapse (Supplementary Movie S22); epithelial domes were scored between 72–96 h (Supplementary Movies S22–23). Dome formation index: fraction of fields containing domes over time. Mean ± SD (n = 24 fields; 3 independent experiments). **g**. Fixed-sample dome proxy. Jammed SCR and IRSp53_KD monolayers (GFP–E-cadherin lines) fixed at 96 h and stained for F-actin (TRITC–phalloidin) and DAPI (β-catenin and GFP–E-cadherin visualizations not shown). Bar, 100 µm. Holes within the epithelial layer were used as a proxy for domes. Dome formation index: domes/field, normalized to SCR mean. Mean ± SD (n = 28 fields; 2 independent experiments). Statistical tests are in Supplementary Table 4, P values are in the graphs.

https://doi.org/10.1038/s41563-026-02553-2

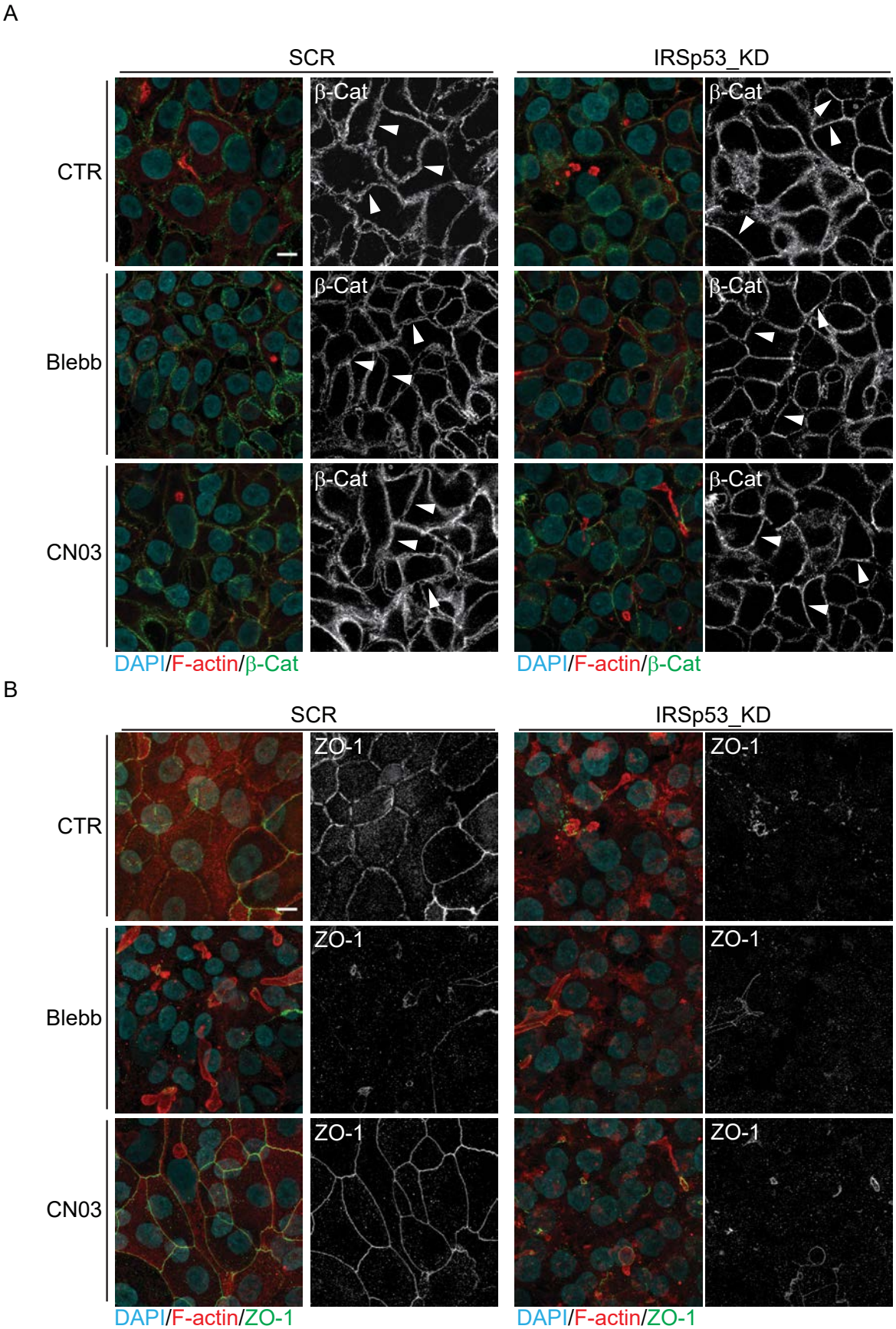

Extended Data Fig. 6 | See next page for caption.

https://doi.org/10.1038/s41563-026-02553-2

Extended Data Fig. 6 | Morphological analysis of cell junctions in control and IRSp53 silenced monolayers. a. Confocal microscopy image sections (5 µm from the bottom adherent surface) of SCR and IRSp53_KD MCF10DCIS.com cells seeded at jamming density and fixed 96 hours after seeding. 16 h before fixation, cells were treated with DMSO (CTR), 5 µM Blebbistatin or 10 µg/ml CN03. Cells were stained with anti-β-catenin antibody (green), TRITC-phalloidin to detect F-actin (red), and DAPI (blue). Arrowheads indicate the different architecture and thinning of cell-cell junctions highlighted by β-catenin staining. Bar, 10 µm. **b**. Confocal microscopy analysis of doxycycline-treated SCR and IRSp53_KD MCF10DCIS.com cells seeded at jamming density and fixed 96 hours after seeding. 16 h before fixation, cells were treated with DMSO (CTR), 5 µM Blebbistatin or 10 µg/ml CN03. Cells were stained with anti-ZO-1 antibody (green), TRITC-phalloidin to detect F-actin (red), and DAPI (blue). Confocal sections on z axis were acquired with 0.5 µm step-size. Representative maximum projection images are shown. Bar, 10 µm.

https://doi.org/10.1038/s41563-026-02553-2

A

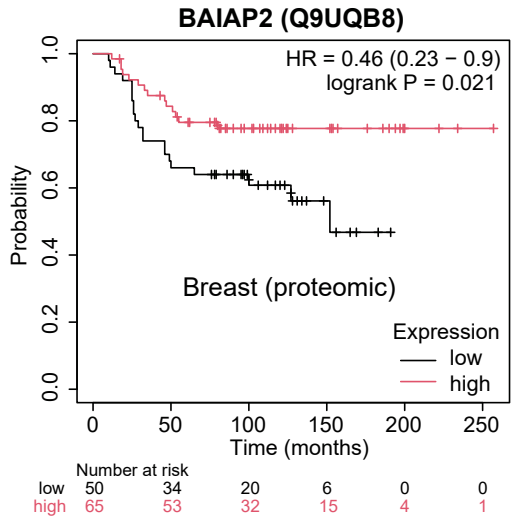

B

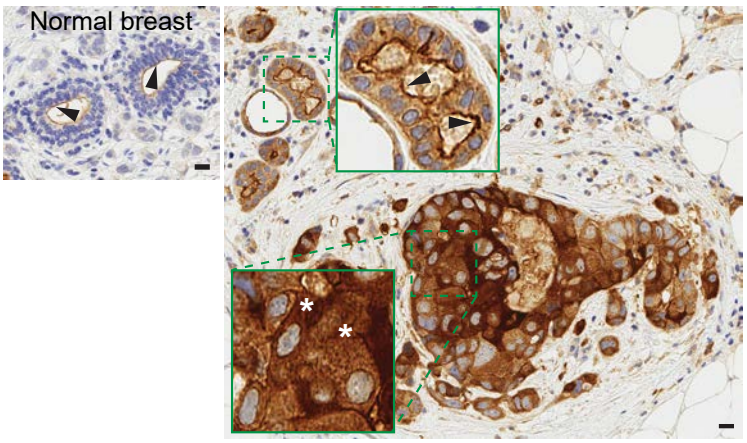

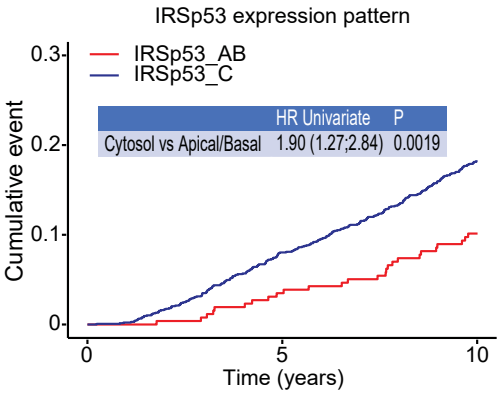

		IRSp53_AB		IRSp53_C				
		N	% row	N	% row	Total	OR (95% CI)	P
ER PGR	Not Exp	11	4.6	231	95.4	242	Ref.	
	Exp	247	17.8	1142	82.2	1389	0.22 (0.12;0.41)	<.0001
HER2	Neg	245	17.4	1163	82.6	1408	Ref.	
	Pos	13	6.3	194	93.7	207	3.14 (1.76;5.60)	<.0001
pN	0	131	17.6	614	82.4	745	Ref.	
	1+	122	14.2	735	85.8	857	1.29 (0.98;1.68)	0.07
	X	5	17.2	24	82.8	29	1.02 (0.38;2.73)	1.00
pT	pT1a/b	36	24.3	112	75.7	148	Ref.	
	pT1c	155	17.4	738	82.6	893	1.53 (1.01;2.31)	0.05
	pT2	58	10.9	474	89.1	532	2.63 (1.65;4.18)	<.0001
	pT3/pT4	9	15.5	49	84.5	58	1.75 (0.78;3.91)	0.19
Subtype	Lum A	85	30.1	197	69.9	282	Ref.	
	Lum B HER2-	148	15.4	814	84.6	962	2.37 (1.74;3.23)	<.0001
	HER2+	13	6.5	187	93.5	200	6.21 (3.35;11.50)	<.0001
	TN	9	5.8	146	94.2	155	7.00 (3.41;14.37)	<.0001
ki67	<14%	126	30.0	294	70.0	420	Ref.	
	>=14%	132	10.9	1078	89.1	1210	3.50 (2.66;4.61)	<.0001
Grade	1	115	42.4	156	57.6	271	Ref.	
	2	106	15.4	584	84.6	690	4.06 (2.96;5.58)	<.0001
	3	33	5.2	602	94.8	635	13.45 (8.79;20.58)	<.0001

Extended Data Fig. 7 | See next page for caption.

https://doi.org/10.1038/s41563-026-02553-2

Extended Data Fig. 7 | IRSp53 low expression and delocalization in breast cancer are significantly associated with poor overall survival. a. Low IRSp53 protein levels significantly correlate with reduced overall survival in breast cancer (https://kmplot.com/ and[2]. **b.** Left, representative IHC images of IRSp53 localization in normal breast (upper left panel) and in normal breast to DCIS progression (right panel). Insets, 2.5x magnifications. IRSp53 at the luminal side of normal breast epithelial cells (black arrowheads). Cytosolic distribution (*) in DCIS. Bar, 20 µm. Right graph, Cytosol distribution significantly correlates with 10-year cumulative incidence of overall survival in the IEO BC cohort (N = 1631) in Univariate analysis. P-value, Wald test. Bottom table, association between IRSp53_AB (apical/basal membrane distribution with a specific elevation on the luminal side) or IRSp53_C (cytosolic distribution) and clinic-pathological parameters was evaluated using the Fisher's exact test. The number (N) of patients and percentage (% row) in each group is indicated. ER PGR, estrogen-progesterone expression; HER, HER gene expression; pN, nodal status; pT, primary tumor size; Subtype, molecular subtype; KI-67, proliferation index; Grade, grade of differentiation; OR odds ratio (95% CI, Confidence Interval); P, p-value.

https://doi.org/10.1038/s41563-026-02553-2

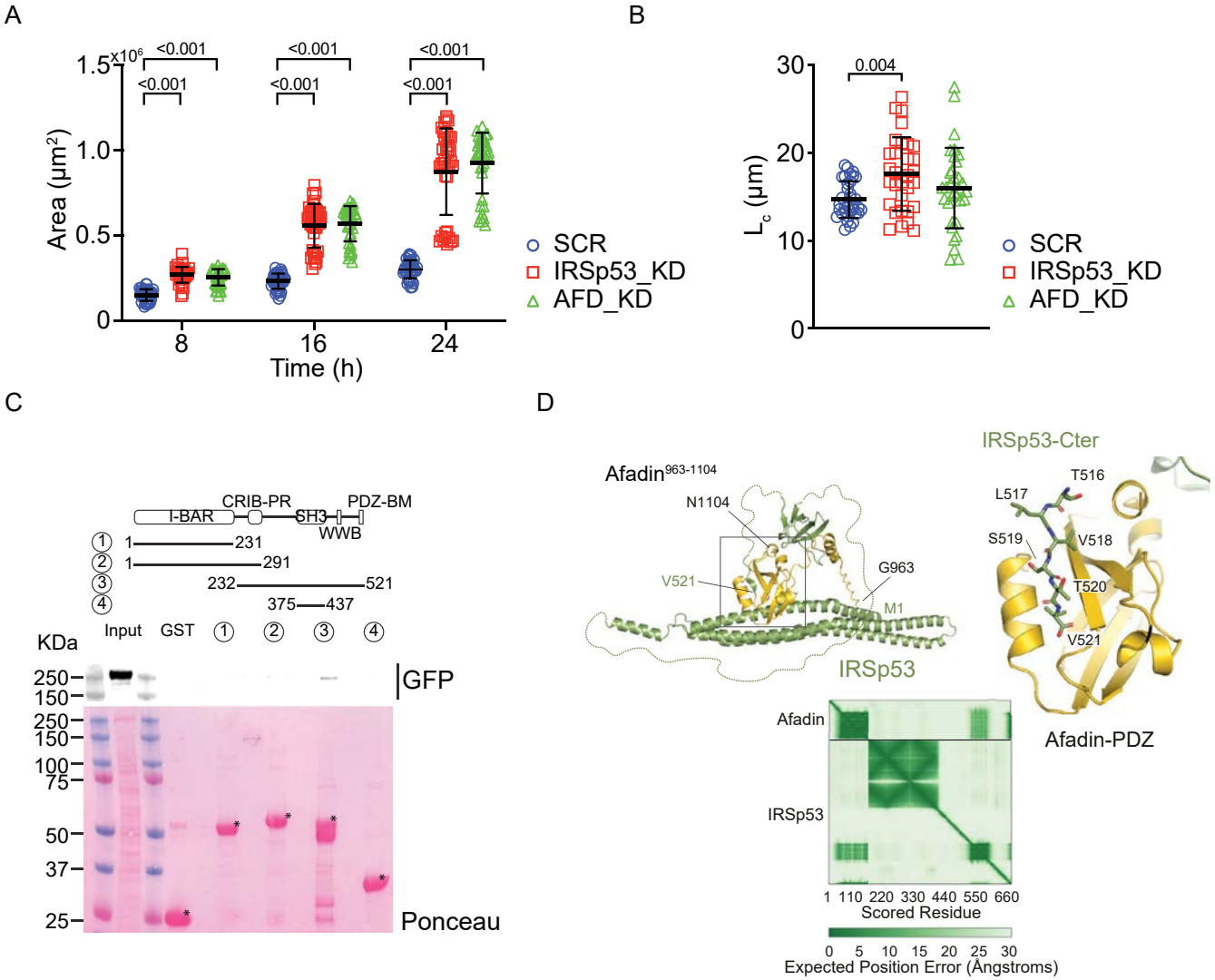

Extended Data Fig. 8 | See next page for caption.

https://doi.org/10.1038/s41563-026-02553-2

Extended Data Fig. 8 | IRSp53 regulates epithelial architecture and spheroids active wetting by recruiting Afadin to cell–cell junctions. a. The spreading area of wetting spheroids (Fig. 6a and Supplementary Movie S24) at the indicated time points was manually quantified using ImageJ. Mean ± SD (n = 38 SCR, 39 IRSp53_KD, 38 AFD_KD spheroids; 3 independent experiments). **b**. Nematic length L_c obtained from image segmentation and PIV analysis of wetting spheroids (Fig. 6a and Supplementary Movie S24). Mean ± SD (n = 34 SCR, 31 IRSp53_KD, 33 AFD_KD spheroids; 3 independent experiments). **c**. Analysis of IRSp53-Afadin surface interaction. Lysates (2 mg) of 293 T cells transfected with GFP-Afadin were incubated with 0.5 µM of immobilized GST–IRSp53 fragment as indicated or GST. Lysates (20 µg) and bound proteins were immunoblotted with anti-GFP antibody. Ponceau staining was employed to detect GST recombinant proteins. **d**. Top left panel, computationally predicted structural model of the IRSp53:Afadin-PDZ domain (963-1104) interaction. Full-length IRSp53 is depicted in green with regions predicted to be unstructured shown as dotted lines, Afadin is in gold. The model was predicted using the AlphaFold3 server (https://alphafoldserver.com/[3]), with overall confidence parameters iPTM = 0.69 and pTM 0.38. Top right panel, close-up view of the putative binding interface between the C-terminus of IRSp53 and the PDZ domain of AFD, showing the canonical PDZ-binding mode of C-terminal hydrophobic peptides. Bottom, Predicted Aligned Error (PAE) matrix for the complex shown in A, with green gradient scale indicating PAE. **e**. Confocal microscopy analysis of doxycycline-treated SCR and IRSp53_KD MCF10DCIS.com cells seeded at jamming density and fixed 96 hours after seeding. Cells were stained with anti-ZO-1 antibody (magenta), anti-AFD antibody (green), TRITC-phalloidin to detect F-actin (red), and DAPI (blue). Confocal sections on z axis were acquired with 0.5 µm step-size. Representative maximum projection images are shown. Arrowheads indicate the localization of AFD and ZO-1 at cell-cell junctions in SCR monolayer. Bar, 10 µm. Statistical tests are in Supplementary Table 4, P values are in the graphs.

https://doi.org/10.1038/s41563-026-02553-2

Multiscale consequences of IRSp53 depletion on epithelial mechanics. Loss of IRSp53 alters Afadin localization and activity. It also results in altered cortical and membrane tension, reduced junctional contractility, and impairs cytoskeletal architecture. These changes compromise supracellular coordination and cell–cell friction, as shown by diminished interdigitating membrane protrusions through ultrastructural EM experiments. Collectively, this lowers spheroid viscosity and enhances active wetting dynamics.

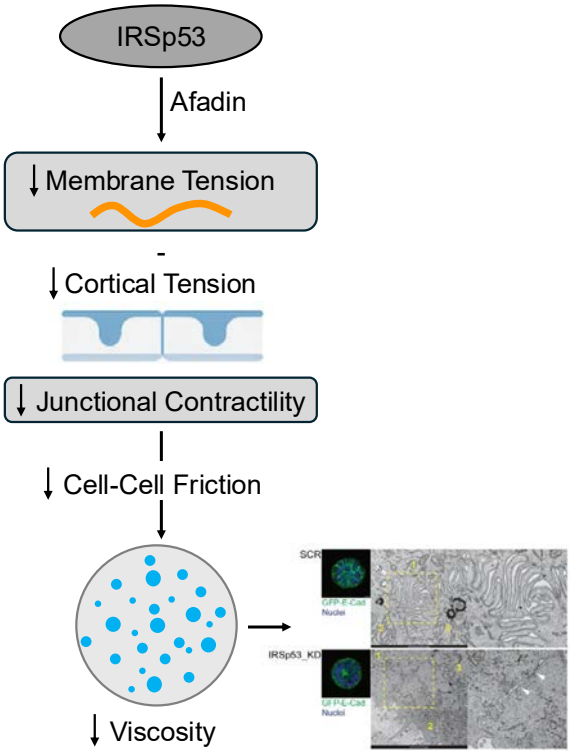

Extended Data Fig. 9 | Conceptual model linking IRSp53-regulated molecular and mechanical parameters across multiple spatial scales to collective migration behaviour. Schematic representation of how IRSp53 depletion impacts collective migration dynamics by perturbing interconnected mechanical and organizational parameters at multiple scales. At the molecular level, IRSp53 modulates the localization and function of junctional proteins such as Afadin, affecting actin organization and cortical contractility. At the cellular level, this results in altered membrane tension, reduced cortical mechanics (as measured by AFM), and weakened adhesion junctional recoil (via laser ablation). At the supracellular level, these changes manifest as diminished junctional line tension, reduced cohesion and morphological order, and decreased friction between cells. Collectively, these alterations compromise the bulk mechanical integrity of the tissue (for example, reduced Young's modulus in spheroids), impairing coordinated force transmission and facilitating unconfined, isotropic wetting behaviour upon IRSp53 loss. The biophysical model parameters—contractility, nematic length, and effective viscosity—are thereby mapped onto experimental readouts such as monolayer stiffness, cell polarity alignment, and spheroid spreading velocity.

nature portfolio

Corresponding author(s): Giorgio Scita & Andrea Disanza & Fabio Giavazzi

Last updated by author(s): Mar 3, 2025

Reporting Summary

Nature Portfolio wishes to improve the reproducibility of the work that we publish. This form provides structure for consistency and transparency in reporting. For further information on Nature Portfolio policies, see our Editorial Policies and the Editorial Policy Checklist.

Statistics

For all statistical analyses, confirm that the following items are present in the figure legend, table legend, main text, or Methods section.

n/a	Confirmed	
☐	☒	The exact sample size (*n*) for each experimental group/condition, given as a discrete number and unit of measurement
☐	☒	A statement on whether measurements were taken from distinct samples or whether the same sample was measured repeatedly
☐	☒	The statistical test(s) used AND whether they are one- or two-sided *Only common tests should be described solely by name; describe more complex techniques in the Methods section.*
☒	☐	A description of all covariates tested
☐	☒	A description of any assumptions or corrections, such as tests of normality and adjustment for multiple comparisons
☐	☒	A full description of the statistical parameters including central tendency (e.g. means) or other basic estimates (e.g. regression coefficient) AND variation (e.g. standard deviation) or associated estimates of uncertainty (e.g. confidence intervals)
☐	☒	For null hypothesis testing, the test statistic (e.g. *F*, *t*, *r*) with confidence intervals, effect sizes, degrees of freedom and *P* value noted *Give P values as exact values whenever suitable.*
☒	☐	For Bayesian analysis, information on the choice of priors and Markov chain Monte Carlo settings
☒	☐	For hierarchical and complex designs, identification of the appropriate level for tests and full reporting of outcomes
☒	☐	Estimates of effect sizes (e.g. Cohen's *d*, Pearson's *r*), indicating how they were calculated

Our web collection on statistics for biologists contains articles on many of the points above.

Software and code

Policy information about availability of computer code

Data collection

- Leica LAS AF
- Olympus CellSens
- Metamorph (v 7.8)
- Nikon Ti2 Control
- Leica Application Suite X (ver. 3.5.2.18963) (Leica SP8 and Leica Thunder)
- Leica Application Suite X (ver. 4.7.0.28176) (Leica Stellaris DIVE)
- EVOS FL software
- Cytiva SoftWorx (7.2.0)
- Zeiss Atlas3D package
- FlowJo v10 (LLC)
- ChemiDoc Imagers (BioRad)
- Invitrogen™ iBright™ Imagers (Thermo Fisher Scientifics)
- Applied Biosystems 7500 (v2.0.6)

Data analysis

- Fiji (v 2.3.0)
- MatLab (v R2021b)
- GraphPad PRISM (10.4.1)
- Excel (16.94)
- SymPhoTime64 (Picoquant)
- C++
- R (v 3.5.2)

- CellProfiler 4
- Image Lab (6.1.0)
- Invitrogen iBright Analysis (5.1.0)

For manuscripts utilizing custom algorithms or software that are central to the research but not yet described in published literature, software must be made available to editors and reviewers. We strongly encourage code deposition in a community repository (e.g. GitHub). See the Nature Portfolio guidelines for submitting code & software for further information.

Data

Policy information about availability of data

All manuscripts must include a data availability statement. This statement should provide the following information, where applicable:

- Accession codes, unique identifiers, or web links for publicly available datasets
- A description of any restrictions on data availability
- For clinical datasets or third party data, please ensure that the statement adheres to our policy

Provide your data availability statement here.

Research involving human participants, their data, or biological material

Policy information about studies with human participants or human data. See also policy information about sex, gender (identity/presentation), and sexual orientation and race, ethnicity and racism.

Reporting on sex and gender	A retrospective cohort of female breast cancer patients was used
Reporting on race, ethnicity, or other socially relevant groupings	The cohort of female patients of different age all European was employed. Detailed description of the selection criteria and the clinico-pathological characteristics of this cohort have been reported in (Pece, S. et al., EBioMedicine 2019).
Population characteristics	A tissue microarray (TMA) comprising a retrospective consecutive cohort of 1755 female patients, from the European Institute of Oncology in Milan , with complete clinicopathological follow-up, was used. All patients provided written informed consent and underwent surgical procedures. Patients were stratified according to the immunohistochemical pattern distribution of IRSp53 (apical/membrane distribution vs cytosolic distribution) in the primary tumor.
Recruitment	The cohort used was a retrospective consecutive cohort of patients enrolled at IEO between years 1997-2000
Ethics oversight	All patients provided written informed consent and underwent surgical procedures.

Note that full information on the approval of the study protocol must also be provided in the manuscript.

Field-specific reporting

Please select the one below that is the best fit for your research. If you are not sure, read the appropriate sections before making your selection.

☒ Life sciences ☐ Behavioural & social sciences ☐ Ecological, evolutionary & environmental sciences

For a reference copy of the document with all sections, see nature.com/documents/nr-reporting-summary-flat.pdf

Life sciences study design

All studies must disclose on these points even when the disclosure is negative.

Sample size	No statistical methods were used to pre-determine sample sizes, which were chosen based on our previous experience (e.g. Nat Mater (2017) 16, 587-596; Nat Mater (2019) 18, 1252-1263; Nat Commun (2020) Jul 14;11(1):3516). The exact replication numbers, sample sizes and statistical methods are described in detail in the text.
Data exclusions	No data were excluded
Replication	Most of the data were replicated in at least 3 independent experiments with few exceptions (as stated in figure legends and in Methods section) in which data were from two independent experiments.
Randomization	For all the experiments with cells or spheroids, we had two or three genetically distinct groups (SCR vs IRSp53_KD or WT vs IRSp53_KO or SCR vs IRSp53 vs AFD_KD) that were treated equally and randomly. For the CLEM experiment, we selected blindly SCR or IRS-53_KD spheroids identified at the confocal microscope based on GFP-ECad expression.
Blinding	The experiments were evaluated blindly by the operators

Reporting for specific materials, systems and methods

We require information from authors about some types of materials, experimental systems and methods used in many studies. Here, indicate whether each material, system or method listed is relevant to your study. If you are not sure if a list item applies to your research, read the appropriate section before selecting a response.

Materials & experimental systems

n/a	Involved in the study
☐	☒ Antibodies
☐	☒ Eukaryotic cell lines
☐	☐ Palaeontology and archaeology
☐	☒ Animals and other organisms
☒	☐ Clinical data
☒	☐ Dual use research of concern
☒	☐ Plants

Methods

n/a	Involved in the study
☒	☐ ChIP-seq
☐	☒ Flow cytometry
☒	☐ MRI-based neuroimaging

Antibodies

Antibodies used

anti-IRSp53, Giorgio Scita lab (produced in house) WB: 5 ug/ml
anti-vinculin, V9131, Sigma-Aldrich WB: 1:2000, IF: 1:1000
anti-Beta-Catenin, PLA2030, Sigma-Aldrich WB: 1:500, IF: 1:400
anti-GFP WB: 1:1000
anti-FLAG, F3165, Sigma-Aldrich IP: 5 ul/mg of lysate
anti-FLAG, 50-199-1716, Rockland WB: 1:1000
anti-afadin (produced in house) WB: 1:500
anti-CD29 (Integrin beta 1) (TS2/16), 14-0299-82, Bioscience FACS: 1 µg/ml
anti-active-Beta1-Integrin (9EG7), 553715, BD Transduction FACS: 10 µg/ml
anti-ZO1, 402200, Invitrogen IF: 1:400, WB: 1:500
anti-Cingulin, 364401, ThermoFisher WB: 1:500
anti-N-cadherin, 364401, ThermoFisher WB: 1:1000
anti-P-cadherin, 610227, BD Transduction WB: 1:1000
anti-E-cadherin, 610181, BD Transduction WB: 1:1000
anti-E-cadherin HECD1, 13-1700, ThermoFisher FACS: 2 µg/ml

anti-rabbit IgG, HRP-linked antibody, 7074, Cell Signaling WB: 1:2500
anti-mouse IgG, HRP-linked antibody, 7076, Cell Signaling WB: 1:2500
Alexa Fluor 488 Donkey anti rabbit, A-21206, ThermoFisher IF: 1:400
Cy3 Donkey anti rabbit, 711-165-152, Jackson Immunoresearch IF: 1:400
Cy3 Donkey anti mouse, 715-165-150, Jackson Immunoresearch IF: 1:400
Alexa Fluor 488 Donkey anti mouse, A-21202, ThermoFisher FACS: 1:400
Alexa Fluor 488 Donkey anti rat, A-21208, ThermoFisher FACS: 1:400
Phalloidin TRITC, P1951, Sigma-Aldrich IF: 1:50
Phalloidin FITC, P5282, Sigma-Aldrich IF: 1:50
DAPI, D-1306, Thermofisher IF: 1:5000
Flipper-TR, SC020, TebuBio 1 uM for live imaging experiments

Validation

anti-IRSp53, Giorgio Scita lab (produced in house) Nat Cell Biol. 2006 Dec;8(12):1337-47; EMBO J. 2013 Oct 16;32(20):2735-50; Nat Commun. 2020 Jul 14;11(1):3516
anti-vinculin, V9131, Sigma-Aldrich https://www.sigmaaldrich.com/IT/it/product/sigma/v9131
anti-Beta-Catenin, PLA2030, Sigma-Aldrich https://b2b.sigmaaldrich.com/IT/it/product/sigma/pla0230
anti-GFP Nat Commun. 2020 Jul 14;11(1):3516
anti-FLAG, F3165, Sigma-Aldrich https://www.sigmaaldrich.com/IT/it/product/sigma/f3165
anti-FLAG, 50-199-1716, Rockland https://www.fishersci.com/shop/products/dykddddk-polyclonal-antibody-rockland/501991716
anti-afadin (produced in house) Nat Struct Mol Biol. 2016 Feb;23(2):155-63
anti-CD29 (Integrin beta 1) (TS2/16), 14-0299-82, Bioscience https://www.thermofisher.com/antibody/product/CD29-Integrin-beta-1-Antibody-clone-TS2-16-Monoclonal/14-0299-82
anti-active-Beta1-Integrin (9EG7), 553715, BD Transduction https://www.bdbiosciences.com/en-it/products/reagents/flow-cytometry-reagents/research-reagents/single-color-antibodies-ruo/purified-rat-anti-mouse-cd29.553715?tab=product_details
anti-ZO1, 402200, Invitrogen https://www.thermofisher.com/antibody/product/ZO-1-Antibody-Polyclonal/40-2200
anti-Cingulin, 364401, ThermoFisher https://www.thermofisher.com/order/catalog/product/364401
anti-N-cadherin, 364401, ThermoFisher https://www.bdbiosciences.com/en-ch/products/reagents/microscopy-imaging-reagents/immunofluorescence-reagents/purified-mouse-anti-n-cadherin.610920?tab=product_details
anti-P-cadherin, 610227, BD Transduction https://www.bdbiosciences.com/en-us/products/reagents/microscopy-imaging-reagents/immunofluorescence-reagents/purified-mouse-anti-p-cadherin.610227?tab=product_details
anti-E-cadherin, 610181, BD Transduction https://www.bdbiosciences.com/en-ie/products/reagents/microscopy-imaging-reagents/immunofluorescence-reagents/purified-mouse-anti-e-cadherin.610181?tab=product_details
anti-E-cadherin HECD1, 13-1700, ThermoFisher https://www.thermofisher.com/antibody/product/E-cadherin-Antibody-clone-HECD-1-Monoclonal/13-1700

anti-rabbit IgG, HRP-linked antibody, 7074, Cell Signaling https://www.cellsignal.com/products/secondary-antibodies/anti-rabbit-igg-hrp-linked-antibody/7074?srsltid=AfmBOorcmvNOeAa8l-uJrlZeKPo8WwHd2PUyhtxDR4oHgQJSYjzKATm5
anti-mouse IgG, HRP-linked antibody, 7076, Cell Signaling https://www.cellsignal.com/products/secondary-antibodies/anti-mouse-igg-hrp-linked-antibody/7076?srsltid=AfmBOorT5sBMJyB6N4obhmF6KPauOWLEzdd6pjJwu-arxq-r2Eq-iXle

Alexa Fluor 488 Donkey anti rabbit, A-21206, ThermoFisher https://www.thermofisher.com/antibody/product/Donkey-anti-Rabbit-IgG-H-L-Highly-Cross-Adsorbed-Secondary-Antibody-Polyclonal/A-21206
Cy3 Donkey anti rabbit, 711-165-152, Jackson Immunoresearch https://www.jacksonimmuno.com/catalog/products/711-165-152
Cy3 Donkey anti mouse, 715-165-150, Jackson Immunoresearch https://www.jacksonimmuno.com/catalog/products/715-165-150
Alexa Fluor 488 Donkey anti mouse, A-21202, ThermoFisher https://www.thermofisher.com/antibody/product/Donkey-anti-Mouse-IgG-H-L-Highly-Cross-Adsorbed-Secondary-Antibody-Polyclonal/A-21202
Alexa Fluor 488 Donkey anti rat, A-21208, ThermoFisher https://www.thermofisher.com/antibody/product/Donkey-anti-Rat-IgG-H-L-Highly-Cross-Adsorbed-Secondary-Antibody-Polyclonal/A-21208
Phalloidin TRITC, P1951, Sigma-Aldrich https://www.sigmaaldrich.com/IT/it/product/sigma/p1951?srsltid=AfmBOoqkXujDb3XkGgJEpL8DDcSBN9PNzWuV44cslp6tS9wq4Y18ZQp8
Phalloidin FITC, P5282, Sigma-Aldrich https://www.sigmaaldrich.com/IT/it/product/sigma/p5282?srsltid=AfmBOopIh9FyB6w8Uupsw3mK0x9hEOMFhYs87jOKBwM3FmcvnYXxdbJK
DAPI, D-1306, Thermofisher https://www.thermofisher.com/order/catalog/product/D1306
Flipper-TR, SC020, TebuBio https://www.tebubio.com/it-eur/flipper-tr/5637154350.p

Eukaryotic cell lines

Policy information about cell lines and Sex and Gender in Research

Cell line source(s)	- MCF10.DCIS.com cells were provided by J. F. Marshall (Barts Cancer Institute, Queen Mary University of London, UK) and maintained in DMEM/F12 (Gibco) supplemented with 5% horse serum (Life Technologies), 2 mM L-Glutamine (EuroClone), 0.5 mg/ml Hydrocortisone (Sigma-Aldrich), 10µg/ml Human insulin (Sigma-Aldrich) and 20ng/ml EGF (Peprotech). - HaCaT (ATCC) were maintained DMEM (Lonza) + 10% FBS (Life Technologies) + 2 mM L-Glutamine (EuroClone). - MECs (Mammary Gland Epithelial Cells) derived from mouse mammary gland were maintained in MEGM medium (CC-3150, Lonza). - Phoenix-AMPHO cells (American Type Culture Collection, CRL-3213) were used as the packaging cell line for the generation of retroviral particles and cultured as recommended by the supplier. - HEK293T (BBCF-Biological Bank and Cell factory, INT, Milan) were grown in DMEM (Lonza) supplemented with 10% FBS (Life Technologies) and 2 mM L-Glutamine (EuroClone) and used as the packaging line for lentiviral vectors.
Authentication	The identity of each of the cell line was verified by fingerprinting by our cell culture facility.
Mycoplasma contamination	Each of the cell line is tested negative for Mycoplasma by our cell culture facility.
Commonly misidentified lines (See ICLAC register)	No commonly misidentified cell lines were used.

Palaeontology and Archaeology

Specimen provenance	*Provide provenance information for specimens and describe permits that were obtained for the work (including the name of the issuing authority, the date of issue, and any identifying information). Permits should encompass collection and, where applicable, export.*
Specimen deposition	*Indicate where the specimens have been deposited to permit free access by other researchers.*
Dating methods	*If new dates are provided, describe how they were obtained (e.g. collection, storage, sample pretreatment and measurement), where they were obtained (i.e. lab name), the calibration program and the protocol for quality assurance OR state that no new dates are provided.*

☐ Tick this box to confirm that the raw and calibrated dates are available in the paper or in Supplementary Information.

Ethics oversight	*Identify the organization(s) that approved or provided guidance on the study protocol, OR state that no ethical approval or guidance was required and explain why not.*

Note that full information on the approval of the study protocol must also be provided in the manuscript.

Animals and other research organisms

Policy information about studies involving animals; ARRIVE guidelines recommended for reporting animal research, and Sex and Gender in Research

Laboratory animals	We employed C57Bl/6J female mice (7-10 weeks old), either wild type or KO for IRSp53 (EMBO J (2013) 32, 2735-2750) . The animals were housed at 20-24 degrees in controlled humidity ranging from 45 to 60% and with a12 hours light cycle in a certified animal facility under the control of the institutional organism for animal welfare and ethical approach to animals in experimental procedures (Cogentech OPBA) Methods used with these animals: Animals were euthanized with a high concentration of CO2 and mammary glands were excised post mortem.
Wild animals	No wild animals were used in the study.

Reporting on sex	Only female animals were employed since we derived Mammary Gland primary cells
Field-collected samples	No field-collected samples were used in the study.
Ethics oversight	All animal experiments were approved by the institutional organism for animal welfare and ethical approach to animals in experimental procedures (Cogentech OPBA). All animal studies were conducted with the approval of Italian Minister of Health (1192/2020-PR) and were performed in accordance with the Italian law (D.lgs. 26/2014), which enforces Dir. 2010/63/EU (Directive 2010/63/EU of the European Parliament and of the Council of 22 September 2010 on the protection of animals used for scientific purposes)

Note that full information on the approval of the study protocol must also be provided in the manuscript.

Plants

Seed stocks	*Report on the source of all seed stocks or other plant material used. If applicable, state the seed stock centre and catalogue number. If plant specimens were collected from the field, describe the collection location, date and sampling procedures.*
Novel plant genotypes	*Describe the methods by which all novel plant genotypes were produced. This includes those generated by transgenic approaches, gene editing, chemical/radiation-based mutagenesis and hybridization. For transgenic lines, describe the transformation method, the number of independent lines analyzed and the generation upon which experiments were performed. For gene-edited lines, describe the editor used, the endogenous sequence targeted for editing, the targeting guide RNA sequence (if applicable) and how the editor was applied.*
Authentication	*Describe any authentication procedures for each seed stock used or novel genotype generated. Describe any experiments used to assess the effect of a mutation and, where applicable, how potential secondary effects (e.g. second site T-DNA insertions, mosiacism, off-target gene editing) were examined.*

Flow Cytometry

Plots

Confirm that:

☐ The axis labels state the marker and fluorochrome used (e.g. CD4-FITC).

☐ The axis scales are clearly visible. Include numbers along axes only for bottom left plot of group (a 'group' is an analysis of identical markers).

☐ All plots are contour plots with outliers or pseudocolor plots.

☒ A numerical value for number of cells or percentage (with statistics) is provided.

Methodology

Sample preparation	For FACS-based quantification of cell surface E-Cadherin (ECAD), active β1-integrin, and total β1-integrin, adherent SCR and IRSp53_KD cells were labeled in vivo at 4°C with anti-ECAD (HECD-1) at 2µg/mL, anti-active β1-integrin (9EG7) at 10µg/mL, or anti-total β1-integrin (TS2/16) at 1µg/mL for 1 hour, followed by incubation with anti-mouse (for ECAD and total β1-integrin) or anti-rat (for active β1-integrin) Alexa-488 conjugated secondary antibody for 30 minutes at 4°C. Cells were then washed with ice-cold PBS 1x, detached using 0.25% trypsin, subsequently fixed with 2% formaldehyde in PBS on ice for 15 min. After fixation, cells were washed and resuspended in PBS supplemented with 2 mM EDTA and further processed for FACS analysis using a BD FacsCelesta. Analysis was performed using FlowJo software (LLC). Cell doublets and clumps were excluded by analyzing the side scatter area (SSC) versus the height peak parameter.
Instrument	BD FacsCelesta.
Software	FlowJo
Cell population abundance	All cells were included in the analysis
Gating strategy	Cells with the correct morphology were selected using the forward scatter area (FSC) versus SSC area parameters. The mean fluorescence intensity of surface proteins in SCR and IRSp53_KD samples was extrapolated, subtracted from background (i.e., the mean fluorescence intensity from cells labeled with the secondary antibody alone) and normalized to SCR sample

☐ Tick this box to confirm that a figure exemplifying the gating strategy is provided in the Supplementary Information.